







Evidence for Intrinsic X-ray Weakness Among Red Quasars at Cosmic Noon

YILUN MA (马逸伦) ¹, ANDY GOULDING ¹, JENNY E. GREENE ¹, NADIA L. ZAKAMSKA ²,
DOMINIKA WYLEZALEK ³ AND YAN-FEI JIANG (姜燕飞) ⁴

¹*Department of Astrophysical Sciences, Princeton University, Princeton, NJ 08544, USA*

²*Department of Physics & Astronomy, Johns Hopkins University, Baltimore, MD 21218, USA*

³*Zentrum für Astronomie der Universität Heidelberg, Astronomisches Rechen-Institut,
Mönchhofstraße 12-14, D-69120 Heidelberg, Germany*

⁴*Center for Computational Astrophysics, Flatiron Institute, New York, NY 10010, USA*

(Received December 8th, 2023; Revised August 4th, 2024; Accepted August 6th, 2024)

Submitted to ApJ

ABSTRACT

Quasar feedback is a key ingredient in shaping galaxy evolution. A rare population of extremely red quasars (ERQs) at $z = 2 - 3$ are often associated with high-velocity [O III] λ 5008 outflows and may represent sites of strong feedback. In this paper, we present an X-ray study of 50 ERQs to investigate the link between the X-ray and outflow properties of these intriguing objects. Using hardness ratio analysis, we confirm that the ERQs are heavily obscured systems with gas column density reaching $N_{\text{H}} = 10^{23-24} \text{ cm}^{-2}$. We identify 20 X-ray-non-detected ERQs at high mid-infrared luminosities of $\nu L_{\nu, 6\mu\text{m}} \gtrsim 3 \times 10^{46} \text{ erg s}^{-1}$. By stacking the X-ray observations, we find that the non-detected ERQs are on average underluminous in X-rays by a factor of ~ 10 for their mid-infrared luminosities. We consider such X-ray weakness to be due to both heavy gas absorption and intrinsic factors. Moreover, we find that the X-ray-weak sources also display higher-velocity outflows. One option to explain this trend is that weaker X-rays facilitate more vigorous line-driven winds, which then accelerate the [O III]-emitting gas to kpc-scales. Alternatively, super-Eddington accretion could also lead to intrinsic X-ray weakness and more powerful continuum-driven outflow.

Keywords: Quasars (1319), Supermassive black holes (1663), X-ray quasars (1821)

1. INTRODUCTION

It has been long thought that the supermassive black holes (SMBHs) at the center of galaxies could significantly impact and coevolve with their hosts via feedback processes (e.g., King 2003; Veilleux et al. 2005; Heckman & Best 2014). These feedback processes may be responsible for the high-end cutoff of the galaxy luminosity function (Croton et al. 2006) and the required rapid quenching mechanisms to produce the observed massive quiescent galaxy populations at high redshift (e.g., Girelli et al. 2019; Ito et al. 2023). For example, accreting SMBHs can become luminous enough to launch

galactic outflows that are capable of removing gas and therefore quenching the star formation of the host galaxy (Silk & Rees 1998; Hopkins et al. 2006). This is often referred to as “quasar-mode” feedback. Observationally, the presence of quasar-driven outflows and winds is often inferred from blueshifted and/or asymmetric emission or absorption line profiles in both spatially unresolved and resolved spectroscopic observations (e.g., Cano-Díaz et al. 2012; Greene et al. 2012; Harrison et al. 2016; Förster Schreiber et al. 2019; Leung et al. 2019).

Both the cosmic star formation rate density and quasar activities peak at $z = 2 - 3$, a period also known as “Cosmic Noon” (Boyle & Terlevich 1998; Madau & Dickinson 2014). Feedback is thus believed to be the strongest during this period. Indeed, in this redshift range, a population of extremely red quasars (ERQs) is identified based on their high infrared-to-

optical ratios and high rest equivalent width of ultraviolet emission lines (Ross et al. 2015; Hamann et al. 2017). These ERQs are often found to host extreme ionized [O III] λ 5008 outflows up to $|\Delta v| \approx 1500 \text{ km s}^{-1}$, unmatched by any other quasar populations (Zakamska et al. 2016; Perrotta et al. 2019). Thus, despite their rarity (Hamann et al. 2017), ERQs represent the perfect sites to study strong feedback at the peak of quasar activity in cosmic time. Consequently, extensive multi-wavelength observations have been carried out for the intriguing ERQ population across the electromagnetic spectrum (e.g., Alexandroff et al. 2018; Hwang et al. 2018; Vayner et al. 2021; Ishikawa et al. 2021; Vayner et al. 2023). Moreover, recent *James Webb Space Telescope* (*JWST*) observation reveals that at least some ERQs are signposts of protocluster formation (Wylezalek et al. 2022), leaving the environmental effects on this quasar population an open front of investigation.

Based on their unique colors and extreme outflows/winds at different scales, the ERQs may also be the rare examples of luminous super-Eddington accretors at Cosmic Noon (see Alexandroff et al. 2018), but no consensus on the black hole masses of the ERQs has been reached yet (Perrotta et al. 2019; Zakamska et al. 2019). Moreover, another challenge is to determine the bolometric luminosity of the ERQs given their obscured nature. X-ray observations therefore become particularly useful to gauge the level of circumnuclear obscuration and estimate the intrinsic luminosities of these targets. Goulding et al. (2018) conducted a pilot X-ray study on 11 ERQs (10 at $z > 2$ and 1 at $z \sim 1.5$) with confirmed [O III] outflows and/or usable observations from *XMM-Newton* and *Chandra X-ray Observatory* at the time. All 11 ERQs yield significant detections, and both X-ray spectroscopy and hardness ratio analysis suggest that all are heavily obscured sources with $N_{\text{H}} \approx 10^{23} \text{ cm}^{-2}$. Having been corrected for gas absorption, these ERQs appear to be intrinsically as luminous in X-ray as the unobscured quasars at similar mid-infrared luminosities. Intriguingly, given that quasars with strong radiatively-driven outflows tend to be weak in X-ray (e.g., Luo et al. 2014; Ricci et al. 2017), two questions then emerge from these results: 1) what is the driving mechanisms of the extreme outflows in ERQs? 2) does there exist a population of X-ray weak ERQs?

In this work, we present our analysis of a more extensive X-ray sample of 40 ERQs in addition to the Goulding et al. (2018) targets in an attempt to answer the questions above. §2 introduces our samples, X-ray observation with *Chandra*, ground-based spectroscopic observations in the rest-frame optical, and their respective

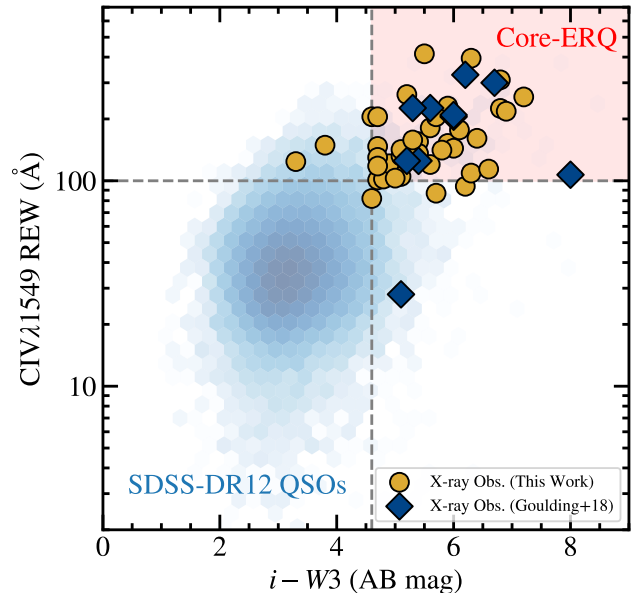


Figure 1. The selection criteria of the ERQ population. The blue hexagons are adopted from the SDSS DR12 QSO catalog.

data reduction procedures. §3 specifies our procedures for spectroscopic and X-ray analysis. §4 lists our results. We then discuss the results and their further implications in §5 and conclude in §6. Throughout the paper, we assume a $H_0 = 70 \text{ km s}^{-1} \text{ Mpc}^{-1}$, $\Omega_m = 0.3$, and $\Omega_\Lambda = 0.7$ cosmology. The emission lines are identified by their vacuum wavelengths.

2. SAMPLE, OBSERVATION, AND DATA REDUCTION

2.1. ERQ Parent Sample

A population of 65 ERQs was first identified by Ross et al. (2015) for their high infrared-to-optical flux ratio ($r_{\text{AB}} - W_{4\text{Vega}} > 14 \text{ mag}$) by cross-matching quasar catalogues of Sloan Digital Sky Survey (SDSS) and Baryonic Oscillation Spectroscopic Survey (BOSS; Dawson et al. 2013, Pâris et al. 2014) to that of the *Wide-Field Infrared Survey Explorer* (*WISE*). The redshift of these quasars ranges over $0.3 \lesssim z \lesssim 4.4$, peaking at $z \sim 0.8$ and $z \sim 2.5$. In the UV wavelengths, the population shows many intriguing spectroscopic properties such as wingless CIV λ 1549 profiles, peculiar emission line ratios, and features of both type-1 (unobscured; e.g., broad permitted lines) and type-2 (obscured; e.g., continuum suppression) quasars. It is therefore not possible to place the whole ERQ population into either type-1 or type-2 quasars, although the presence of broad lines often implies that this intermediate population is more type-1-like.

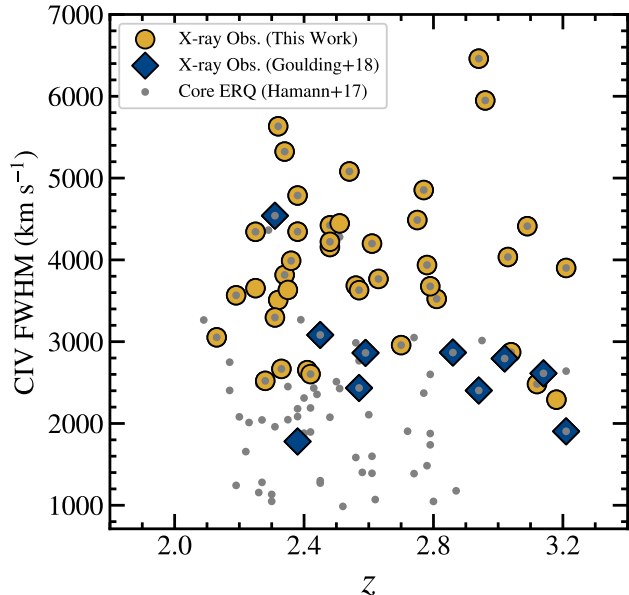


Figure 2. The sample of ERQ targets with X-ray observations is complete for $\text{FWHM}(\text{C IV}) > 3500 \text{ km s}^{-1}$. The gray dots are the core-ERQ sources from Hamann et al. (2017). Note that the blue diamond at $z \approx 3.2$ is SDSS J212951.40–001804.3: Hamann et al. (2017) classified it as ERQ-like in its original catalog due to non-detection in W3; however, Goulding et al. (2018) point out that this source fulfills the core-ERQ the requirement if one uses the most up-to-date *WISE* photometry.

Using the BOSS quasar catalogue for Data Release 12 (DR12Q; Páris et al. 2014, 2017), Hamann et al. (2017) refined the definition of ERQs based on color and rest equivalent width (REW) of the $\text{C IV } \lambda 1549$ lines. Primarily, ERQs are selected by their red colors, i.e. $i - W3 \geq 4.6 \text{ mag}$ (AB magnitude). Furthermore, a core subsample of 97 ERQs, dubbed “core-ERQs”, is identified by $\text{REW}(\text{C IV}) \geq 100 \text{ \AA}$ at $2 < z < 3.4$ by the similarity of their distinctive emission-line properties and shapes of the spectral energy distribution (SED). We show the selection of core-ERQs and their comparison with the SDSS-DR12 QSOs at $2 < z < 3$ in Figure 1. Hamann et al. (2017) also expand the samples to include 235 “ERQ-like” quasars that meet either of the two “core” criteria mentioned above or whose C IV profile is wingless/boxy inferred from the line profile’s kurtosis measurements. For the rest of the paper, we make no distinction between core and ERQ-like targets and dub both sub-populations “ERQs”, since the majority of our sample is drawn from the core population and only six sources are significantly outside of the core-ERQ selection box (see Figure 1 and § 2.2 below).

2.2. ERQ X-Ray Sample and Observation

In order to measure the full SED and potentially estimate bolometric luminosity, probe circumnuclear obscuration level of the ERQs, and to link the X-ray properties to the high-velocity outflows in these systems, we proposed *Chandra* observations (PI: A. Goulding) in Cycle 22 for 23 ERQ targets with $\text{FWHM}(\text{C IV}) \gtrsim 3500 \text{ km s}^{-1}$ and no scientifically usable archival X-ray data at the time. The selection using C IV instead of $[\text{O III}]$ is due to the lack of rest-frame optical spectra for all the targets. However, the asymmetric profile and the broad line width of the $\text{C IV } \lambda 1549$ line hint at the presence of winds (Hamann et al. 2017; Alexandroff et al. 2018), so C IV can possibly be used to estimate the velocity of $[\text{O III}]$ -emitting outflow (see § 4.2) if the two gases are coupled. All targets were approved and observed in the observing cycle. We also cross-matched the *Chandra* archival data against the ERQ catalogue of Hamann et al. (2017) and include 16 more *Chandra* targets on the ACIS-S S3 chip or the ACIS-I chips with mostly snapshot observations ($\sim 4 \text{ ks}$) in addition to our deeper ($\sim 10 - 20 \text{ ks}$) Cycle 22 campaign.

In total, we build an X-ray sample of 40 ERQ targets for this work. We show in Figure 2 that our sample is complete to ERQs with $\text{FWHM}(\text{C IV}) \gtrsim 3500 \text{ km s}^{-1}$. In addition, jointly with 10 ERQs at $z > 2$ studied by Goulding et al. (2018), we probe the X-ray properties of ERQs on the higher end of their outflow velocities. We list both the new X-ray sample (40 ERQs) and the 10 ERQs from Goulding et al. (2018) in Table 1.

For consistency with the analyses of ERQs presented in Goulding et al. (2018), we follow the same processing and data reduction used previously. Briefly, data processing is carried out using the standard *Chandra* X-ray Center software packages in CIAO v4.15 (Fruscione et al. 2006). Consistent calibrations from the CALDB 4.10.2 library are applied using `chandra_repro`. Streak events, bad pixels, pixel randomization and cosmic rays are removed with `STATUS=0` and screened with the typical grad set during the implementation of `acis_process_events`. Flares more than 3σ above the background are identified and removed using the `lc_clean` package before creating final Level-2 events files. Final exposure times in Good Time Intervals are in the range $\sim 4-40 \text{ ks}$. We present the analysis of the reduced *Chandra* X-ray data in § 3.2.

2.3. Ground-Based Near-Infrared Spectroscopy of ERQs

As follow-up observations, we obtained rest-frame optical spectra of 7 ERQs (SDSS J082649.30+163945.2, SDSS J085451.11+173009.1, SDSS J102130.74+214438.4, SDSS J110202.68–000752.7,

SDSS J145623.35+214516.2, SDSS J150117.07+231730.9, and SDSS J154243.87+102001.5) among the X-ray sample using the Folded port InfraRed Echellette (FIRE) spectrograph on the Magellan Baade Telescope, which covers the wavelength range between 0.82 and 2.51 μm . At the redshift of these ERQs, the [O III] $\lambda\lambda$ 4960, 5008 doublet and H β emission lines fall into the observed *H*- or *K*-bands. Depending on the specific redshift of each individual source, we are also able to probe the H γ and/or H α emission of some ERQs. For each target, individual exposures range from 450 s to 1200 s, and the total integration times range from 0.75 h to 1.6 h. We observed all targets with a slit width of 0.75 arcseconds.

We reduce the FIRE spectra using the reduction pipeline `PyPeIt` (Prochaska et al. 2020a,b). The prominent OH emission lines in the spectra are used to calibrate the wavelength solution for each frame. For sources with a bright continuum, we perform automatic extraction in the pipeline. For those with weak continuum, we conduct a semi-automatic routine by manually identifying emission lines in the 2D spectra and therefore guide the code to extract at certain positions along each order of the echellette. The telluric correction and flux calibration are performed using the standard/telluric star spectra observed on the same nights.

Since not all ERQs in the X-ray sample have readily available spectra, we also invoke the rest-frame optical spectra for 28 ERQs taken by Perrotta et al. (2019) in addition to our FIRE observations. This makes a spectroscopic sample of 35 ERQs with available rest-frame optical spectra in total. 19 of the 40 ERQs in our X-ray sample overlap with the spectroscopic sample, and 5 of the 10 ERQs in the X-ray pilot study by Goulding et al. (2018) overlap with this spectroscopic sample.

2.4. Additional HotDOG X-ray Sample as Comparison

Hot dust-obscured galaxies (HotDOGs) are selected to be *WISE* sources with no detection or marginal detections at 3.4 and 4.6 μm but strong detections at 12 and 22 μm likely produced by dust illuminated by the central SMBHs (Eisenhardt et al. 2012; Wu et al. 2012; Bridge et al. 2013). The SEDs of HotDOGs are very similar to those of ERQs, characterized by a relatively flat slope in the UV and a steep rise in the between ~ 1 to 3 microns, but the UV-to-optical continuum is more suppressed and the near-to-mid-infrared rise is steeper in HotDOGs than in the ERQs (Tsai et al. 2015; Hamann et al. 2017). Although selected using different criteria, HotDOGs and ERQs may both represent a similar phase of obscured accretion, with the former being more dust-dominated. Therefore, we include an X-ray sample of 18 HotDOGs from Vito et al. (2018) in

our study. This allows us to probe and compare the X-ray properties of red quasars at even higher luminosities ($\nu L_{\nu, 6 \mu\text{m}}^{\text{HotDOG}} \approx 10^{47-48} \text{ erg s}^{-1}$) than the ERQs ($\nu L_{\nu, 6 \mu\text{m}}^{\text{ERQ}} \approx 10^{46-47} \text{ erg s}^{-1}$). We are not supplemented with rest-frame optical spectra for the HotDOGs; as a population, they do not show as powerful outflows as the ERQs do (Wu et al. 2018; Finnerty et al. 2020). Conducting a detailed analysis of their outflows is beyond the scope of this work.

3. ANALYSIS

3.1. Emission Line Analysis on Rest-Frame Optical and UV Spectra

ERQs show signatures of the most extreme outflows in the universe. Their [O III] emission is so broadened and blueshifted that it is strongly blended with the H β emission (Zakamska et al. 2016; Perrotta et al. 2019). Spectroscopic analysis of ERQs is essential to determine their redshifts and infer the gas kinematics in these sources. Therefore, we conduct multi-component fitting to the ERQs' rest-frame optical and UV spectra.

For ERQs with rest-frame optical spectra available (from either our FIRE observations or Perrotta et al. 2019), we fit the rest-frame optical spectra over the entire observed *H*- and *K*- bands (if available). We characterize the continuum as two independent linear functions in the two bands, respectively. We model the emission line profiles as Gaussians. For each line in the rest-frame optical spectra, we allow there to be a maximum of three kinematic components:

1. a broad component for the permitted lines with full-width-half-maximum (FWHM) $> 2000 \text{ km s}^{-1}$ (Zakamska et al. 2003) to represent the broad-line region (BLR) emission;
2. a narrow component for both permitted and forbidden lines with FWHM $< 2000 \text{ km s}^{-1}$ centered with the BLR component to represent the narrow-line region (NLR) emission – all narrow lines have the same FWHM;
3. a blueshifted component for both permitted and forbidden lines representing any additional velocity component such as outflows.

Within each of the three categories above, we fix the FWHM of all the lines under the assumption that all line emission originates from gas with the same kinematics. For example, if we have H β emission with all three components and an [O III] emission with only the NLR and outflow components, the fitting procedure requires $\text{FWHM}_{\text{BLR}}^{\text{H}\beta} \neq \text{FWHM}_{\text{NLR}}^{\text{H}\beta} = \text{FWHM}_{\text{NLR}}^{\text{[OIII]}}$ and

$\text{FWHM}_{\text{outflow}}^{\text{H}\beta} = \text{FWHM}_{\text{outflow}}^{[\text{O III}]}$. Limited by the signal-to-noise ratio (SNR) in some of the spectra, we also fix the NLR-to-outflow flux ratio across all the lines. This treatment aims to reduce the fitting degeneracy due to the blending of $\text{H}\beta + [\text{O III}]$ (and sometimes $\text{H}\alpha + [\text{N II}]$) complexes. It has been discussed in the literature that $[\text{O III}]$ and $\text{H}\beta$ could be kinematically untied particularly in the strong-outflow regime (Zakamska & Greene 2014; Zakamska et al. 2016) due to processes such as NLR stratification (Osterbrock 1991; Komossa et al. 2008) and therefore a more agnostic procedure may be more suitable for fitting these ERQs. For example, Perrotta et al. (2019) assign no physical meanings (i.e. NLR or BLR) to the Gaussian components in their fits and allow different kinematics for $[\text{O III}]$ and $\text{H}\beta$. However, we find that our NLR/BLR treatment also provides equally reasonable residuals and untying the $[\text{O III}]$ and $\text{H}\beta$ kinematics largely yields no significant improvements for most of our ERQs.

We let the FWHM of the NLR emission be larger than 2000 km s^{-1} in a few ERQ targets in order to capture the full profiles. Based on recent *JWST* observation, the immediate environment of ERQs may be complex and dynamic with companion galaxies and gas clumps in addition to the quasar outflow (Wylezalek et al. 2022). These velocity components may blend and result in line widths larger than those found in typical NLR emissions in our spatially unresolved spectra.

We also allow the Fe II emissions to exist if a BLR component for the Balmer lines is detected; conversely, if Fe II features are identifiable by visual inspection, we consequently add a BLR component for the permitted lines. The Fe II emission is modelled by convolving a Gaussian kernel that has the same FWHM in velocity space with the Véron-Cetty et al. (2004) Fe II template. The continuum, the emission lines, and the Fe II template are fitted simultaneously.

There are sometimes ambiguities in choosing either a single BLR component for $\text{H}\beta$ or a wide blueshifted component for the $[\text{O III}]$ to account for the excess flux between the emission lines. In those cases, we turn to the BLR- $\text{H}\beta$ scenario if the blue wing of the fitted $[\text{O III}]\lambda 5008$ profile never dominates over any of the other kinematics components at any wavelengths. Such ambiguity is accounted for in the systematic errors in FWHM measurements. We show some examples of our fitting for the rest-frame optical spectra in Figure 3.

We also fit the $\text{C IV}\lambda 1549$ emission line of ERQs in both the X-ray and spectroscopic samples using their SDSS spectra. For ERQs with rest-frame optical spectra available, we fit the C IV line with the same number of components as $\text{H}\beta$; otherwise, we fit the emission

line with a maximum of three components as described above. C IV lines show many intriguing properties and hint at the obscured nature of ERQs (Hamann et al. 2017), but their origins in the ERQs remain poorly understood. A UV-emitting disk wind is a possible origin given the C IV is often blueshifted, but most such systems show $\text{REW}(\text{C IV})$ much smaller than that of the ERQs (Richards et al. 2011). Zakamska & Alexandroff (2023) also argue that the C IV lines are likely significantly reprocessed and scattered by the torus skin wind, so they may originate on the intermediate spatial scales between those characteristic of the classical BLR and NLR. Although many lines of evidence have been invoked, the spatial extent and origin of C IV remains ambiguous. Thus, we do not assign physical meanings to any of these components – the goal is to fully capture the shape of the C IV lines. Again, the emission feature and a linear continuum are fitted simultaneously within $\sim 500 \text{ \AA}$ of the C IV line with any absorption features manually masked out. We also show examples of the C IV fitting in Figure 3.

To determine the systemic redshift of the ERQs, we use the centroid of the NLR component of the luminous $[\text{O III}]\lambda 5008$ line that is most likely associated with the host galaxy. For ERQs without a rest-frame optical spectrum, we determine the systemic redshift using the peak of the full C IV profile as our best available estimation. The resonant C IV line could be blueshifted as much as $\sim 500 \text{ km s}^{-1}$ from the true systemic redshift due to potential line-driven winds in the BLR (see Richards et al. 2011, Zakamska & Alexandroff 2023, and references therein). Gillette et al. (2023) find that ERQs tend to show an even higher incidence of blueshifted C IV than blue quasars. However, the result of our study does not significantly depend on the accuracy of redshift measurement.

3.2. X-ray Analysis

To analyze the X-ray data, we bin the *Chandra* images into three observed energy bands: 0.3–1 keV (soft), 1–4 keV (middle), and 4–7 keV (hard), which roughly correspond to 1–3.5 keV, 3.5–14 keV, and 14–24.5 keV in the rest frame of ERQs at $z \sim 2.5$. We then use the CIAO package to conduct aperture photometry in each of the three bands and in the full 0.3–7 keV band. We set the aperture radius to be $2''$ and $8''$ for sources observed on the ACIS-S and ACIS-I chips, respectively. The difference is to account for the size increase of the point spread function (PSF) when the targets are imaged with the ACIS-I instead of ACIS-S chips. The background noise level is estimated in an annulus with inner and outer radii being twice and ten times the aperture radius, re-

spectively. We consider a source to be detected if the binomial no-source probability (Weisskopf et al. 2007) is smaller than 0.0013, which corresponds to 3σ above the background level in the Gaussian approximation.

We use the software package Bayesian Estimation of Hardness Ratios (BEHR; Park et al. 2006) to calculate two hardness ratios defined below:

$$\text{HR}_1 = \frac{C_m - C_s}{C_m + C_s}, \quad (1)$$

$$\text{HR}_2 = \frac{C_h - C_m}{C_h + C_m}, \quad (2)$$

where C_s , C_m , and C_h are the photon count in the soft, middle, and hard bands, respectively. BEHR is particularly advantageous in low-count regimes like this study. The code takes the total photon counts in the source and background regions of each energy band, assumes each photon to be an independent Poisson random variable, and makes posterior draws accordingly irrespective of whether the source is formally detected or not. The non-Gaussian uncertainties are thus propagated correctly. We use a Gaussian quadrature algorithm to calculate the posterior distributions of the HRs with 1000 bins and keep all other parameters as default. This procedure is recommended by the BEHR package document for doing calculations with less than ~ 15 counts in either band.

The HRs serve as probes to approximate the level of obscuration along the line of sight between the source and the observer, which we quantify using the hydrogen column density N_H . We simulate a set of absorbed X-ray spectra using the pre-computed MYTorus tables (Yaqoob 2012), which simulate the reprocessed X-ray emission from a toroidal structure. Motivated by the viewing geometry inferred from spectropolarimetry observations by Alexandroff et al. (2018), we use a MYTorus model consisting of a transmitted zeroth-order power-law continuum and a Compton-scattered continuum. We assume a torus inclination angle of $i = 85^\circ$, a power-law slope of $\Gamma = 1.9$, with the normalization and N_H for all components tied together. We assume a range of column densities from 10^{22} cm^{-2} to 10^{25} cm^{-2} at the source redshift. For completeness, we include an additional Galactic foreground absorption component of $N_H = 10^{20} \text{ cm}^{-2}$. Using the exact foreground value along each line-of-sight is only produces 1–5% changes in the final result. This is because Chandra has little sensitivity at $< 1.5 \text{ keV}$, which is the regime likely affected by foreground N_H . Thus, the foreground virtually has no effect on the results of high-redshift sources.

We fold the simulated spectra through the observing-cycle-dependent ACIS-S/ACIS-I response curves. The

spectra are then fed into the Portable, Interactive Multi-Mission Simulator (PIMMS) to simulate count rates as a function of redshift, which we use to calculate the expected HR_1 and HR_2 as a function of redshift z at the different source column densities N_H . The time-varying response curve of ACIS-S/ACIS-I cause the same HR values to yield different N_H measurements. Similar to the treatment in Goulding et al. (2018), we interpolate the N_H values over a grid of redshift and HR_1 or HR_2 values for each observing cycle involved. We note here that adopting simpler absorbed X-ray spectra such as an absorbed power law rather than the aforementioned MYTorus models to generate these expected HR values yields only ~ 0.05 dex difference in the N_H estimation. As pointed out by Goulding et al. (2018), HR_1 is more sensitive to columns below $\sim 10^{23} \text{ cm}^{-2}$, whereas HR_2 is a more reliable probe for columns that are more Compton-thick ($0.3 - 5 \times 10^{24} \text{ cm}^{-2}$). Therefore, similar to their treatment, we adopt the column density inferred from HR_1 if $\text{HR}_2 \lesssim -0.75$ (i.e. HR_2 is consistent with no absorption at source redshift) but otherwise we adopt the column density inferred from HR_2 . ERQs that are not detected in X-rays have no HR measurements and thus no N_H estimates. The uncertainties on N_H are computed from the N_H values corresponding to the 16th- and 84th-percentile values of the HR posterior distributions.

Using PIMMS and assuming a photon index of $\Gamma = 1.9$, we estimate the rest-frame 2–10 keV absorbed and intrinsic luminosities of our ERQs using their count rates in the observed 0.3–7 keV band and the inferred N_H values. For sources undetected in the full 0.3–7 keV band, we compute the 3σ upper limit of total counts according to Gehrels (1986), which provides correct treatments on confidence levels for small-number events that follow Poisson statistics. We then use the counts and thus flux upper limits to constrain upper limits for the unabsorbed $L_{2-10 \text{ keV}}$ assigning $N_H = 10^{24} \text{ cm}^{-2}$ to represent our ignorance of the columns in these X-ray undetected sources – this choice is also motivated by the possibility that the X-ray-non-detections are due to heavier obscuration. This upper limit also increases with increasing column density that is assumed. We also note that two sources were treated specially. Since SDSS J005044.95–021217.6 is only detected in the full 0.3–7 keV band, no HR and thus N_H can be computed for this source. The HR values obtained from SDSS J134248.86+605641.1 is unable to constrain N_H , as the both HR values are below what the HR values that the N_H grid predicts. Thus, we assume $N_H = 10^{25} \text{ cm}^{-2}$ for these two sources and use this value as an upper limit

on column density to compute an upper limit on its L_X .

4. RESULTS

In this section, we present the results of our joint study of rest-frame UV and optical emission lines and the X-ray properties of the ERQs.

4.1. ERQ Bolometric Luminosity

Bolometric luminosity is vital in quasar studies since it is directly related to the rate of accretion that powers these objects. However, it is uncertain to infer bolometric luminosities from X-rays due to the low photon counts and high column densities. Rest-frame optical spectra are not available for all sources in our sample to estimate bolometric luminosity, either. Both the UV emission lines and the UV continuum are likely suppressed by obscuration and reprocessed by scattering in the circumnuclear materials (Hamann et al. 2017; Alexandroff et al. 2018; Zakamska & Alexandroff 2023). Therefore, we use the mid-infrared (MIR) luminosities to approximate the bolometric luminosities of ERQs in a consistent way since all ERQs have available *WISE* data as part of their selection. For the easiest comparison with previous works, we measure νL_ν at rest-frame 5 and 6 microns for the ERQs by fitting a power law on the *WISE* photometry from the AllWISE source catalog (Wright et al. 2019). These luminosity measurements are presented in Table 1. The MIR light is expected to arise from the isotropic re-emission by the dust surrounding the SMBH and provides the most reliable measure of the bolometric luminosity available to us, although it is possible that light at $6\ \mu\text{m}$ is also suppressed by self-absorption in the torus (Mateos et al. 2015). Richards et al. (2006) find that at 5 or 6 microns, the bolometric correction for type-1 quasars is roughly between 7 and 9, which we adopt to be our estimate.

4.2. ERQ Line Properties

Having settled on the bolometric luminosities, we now present the results from fitting the ERQ spectra. In the rest-frame optical wavelengths, we see a variety of line profiles and spectral features, and a mixture of type-1 and type-2 features is detected (shown in Figure 3). In some ERQs, a simple NLR+outflow model suffices for fitting all emission lines, but many other ERQs require a broad non-blueshifted component for the Balmer lines. We also detect the permitted Fe II multiplet pseudo-continuum in 18 sources. We believe the presence of Fe II and the broad Balmer emissions provide evidence that the BLR in certain ERQs is partially unobscured (see more discussion in § 5.1). We note

that SDSS J154243.87+102001.5 cannot be fitted with a quasar+outflow model. Based on the emission-like feature in its fitting residual, additional velocity components such as companions are potentially present.

In order to compare with previous work, we also measure the line width that encompasses 90% of the total power, $W_{90,\text{line}}$, of the [O III] λ 5008 line for ERQs with available rest-frame optical spectra. The $W_{90,[\text{OIII}]}$ measurements of all but two ERQs are above $2000\ \text{km s}^{-1}$. Although we utilize custom fitting routines in this work, we confirm the very broad [O III] line widths presented in previous studies of ERQs (Zakamska et al. 2016; Perrotta et al. 2019). The two sources with $W_{90,[\text{OIII}]} < 2000\ \text{km s}^{-1}$ are SDSS J082649.30+163945.2, which has a low-SNR spectra, and SDSS J110202.68–000752.7, whose spectra are affected by strong telluric absorption.

Moreover, in the rest-frame UV, we measure the $W_{90,\text{CIV}}$ of all ERQs to be above $3000\ \text{km s}^{-1}$, consistent with those found in blue type-1 quasars (e.g., Baskin & Laor 2005; Sulentic et al. 2017). However, many CIV profiles in our ERQ sample also show non-Gaussian and non-Lorentzian shapes. These findings are all consistent with the line properties found in the original ERQ selection paper (Hamann et al. 2017) and the physical picture in which CIV is partially reprocessed by the outflowing obscuring material (e.g., Richards et al. 2011; Alexandroff et al. 2018; Zakamska et al. 2003). We defer any further discussions of the CIV physics to future work as it is beyond the scope of this paper.

Although the CIV origin remains ambiguous, a relationship between the line widths may exist if the winds traced by the CIV-emitting gas and [O III]-emitting gas are somehow coupled. Such a relation can then be used to estimate $W_{90,[\text{OIII}]}$ for sources without rest-frame optical spectra. Therefore, we fit for a linear $W_{90,[\text{OIII}]} - W_{90,\text{CIV}}$ relationship with ERQs with readily available spectra using the Bayesian linear regression code `linmix` (Kelly 2007) and find

$$W_{90,[\text{OIII}]} = 2.12_{-0.53}^{+0.64} \times W_{90,\text{CIV}} - 5923_{-3199}^{+2683}, \quad (3)$$

where the line widths are in units of km s^{-1} and the errors are the 16th- and 84th-percentiles from the posterior distributions of the slope and the intercept. The best-fit line and the confidence intervals are shown in Figure 4. The fitted intrinsic scatter for the used line widths is $\sigma_{\text{int}} = 1138_{-498}^{+549}\ \text{km s}^{-1}$. We only exclude SDSS J110202.68–000752.7 from the fit since its [O III] λ 5008 line is overwhelmed by telluric absorption and thus its $W_{90,[\text{OIII}]}$ cannot be reliably measured. These line widths have a Pearson correlation coefficient of $\rho = 0.525$ with a p -value of 0.00144. If we were to exclude SDSS J082649.30+163945.2, whose $W_{90,[\text{OIII}]}$

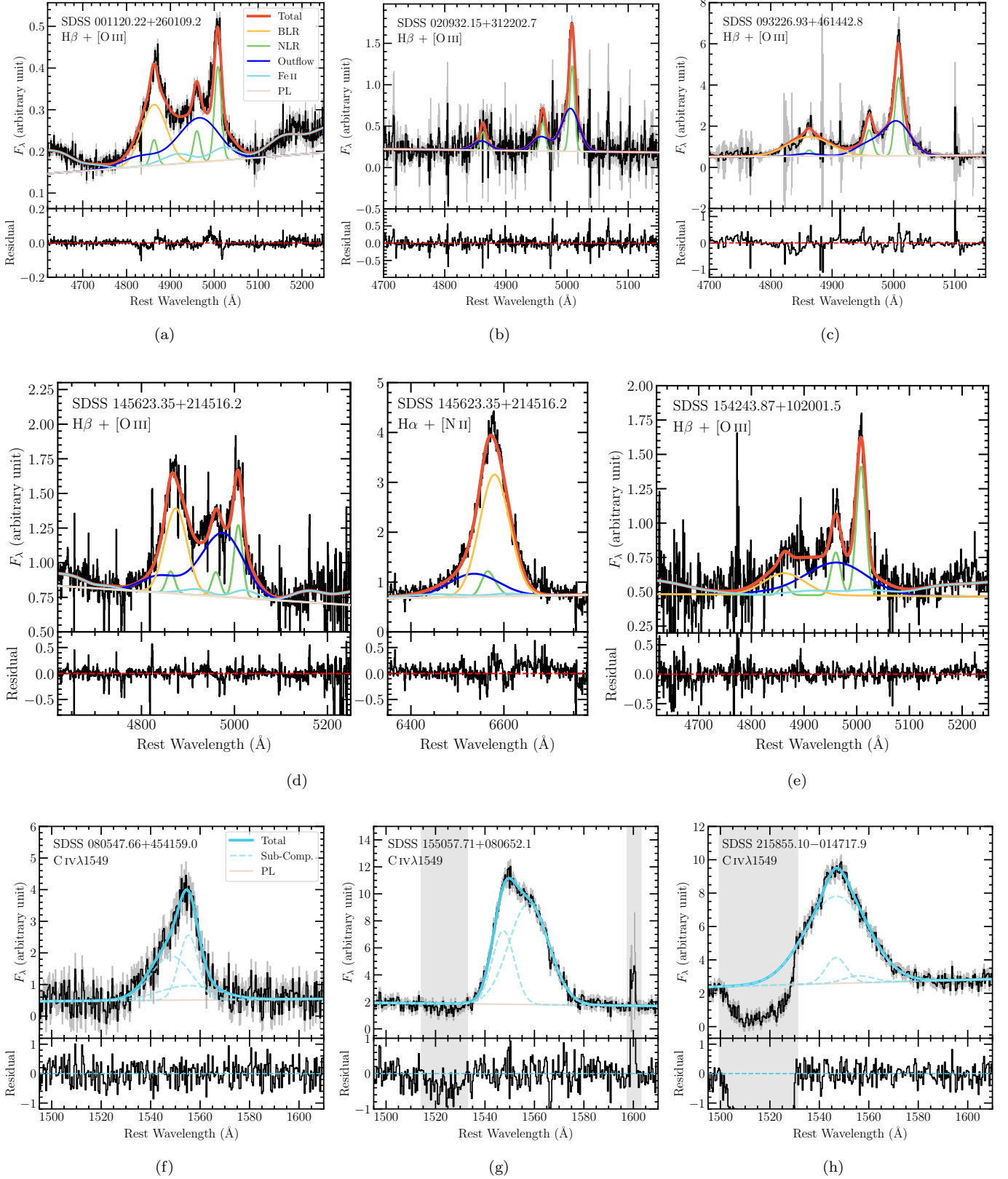


Figure 3. ERQs show diverse emission line morphology. **(a)–(e):** Examples of the multicomponent fit of the $H\beta + [O III]$ complex and $H\alpha$ complex for the ERQs. The total best-fit model is colored red; the yellow, green, and blue curves represent BLR, NLR, and outflow components, respectively; Fe II multiplet is displayed in cyan and the continuum is the pink line. **(f)–(h):** Examples of the multicomponent fit for the $C IV \lambda 1549$; solid curves are the total best-fit, and the dashed curves are the different components used (no physical interpretations are associated with these sub-components); shaded regions are masked out during the fitting process.

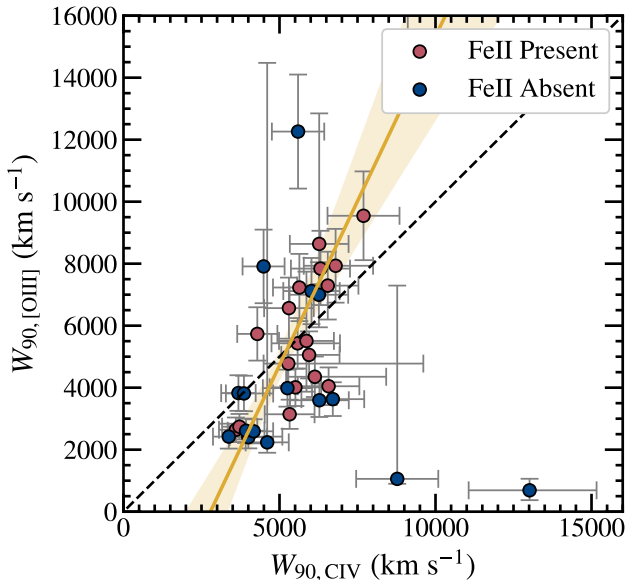


Figure 4. The relationship between the line widths of [O III] λ 5008 and C IV of ERQs, sorted by Fe II presence in the rest-frame optical spectra. The best-fit line is plotted in yellow, and the shaded area marks the 1σ confidence intervals. The dashed line marks the 1 : 1 relation. The point at $W_{90,\text{CIV}} > 10000 \text{ km s}^{-1}$ is J1102–0075 and is not included in the fit due to poor data quality.

may be larger than currently measured from its low-SNR spectrum, we would obtain $\rho = 0.71$ and $p = 4.5 \times 10^{-6}$. Although such calibration may not represent the true [O III] line widths, scaling from C IV to [O III] is the best estimate that we can provide at present given our limited data. All the line width measurements and BLR feature detections are listed in Table 2.

Zakamska & Greene (2014) find a clear positive correlation between the [O III] λ 5008 line width and $12 \mu\text{m}$ luminosities in obscured type-2 quasar at $z < 1$ with $\nu L_{\nu,12\mu\text{m}} \approx 10^{44-46} \text{ erg s}^{-1}$. Zakamska et al. (2016) also find that the line width correlates with $5 \mu\text{m}$ -luminosities as well. The interpretation of such a correlation is that the broadening is due to stronger outflows and winds at higher quasar luminosities. Following this picture, we show in Figure 5 that the ERQs continue to be on this trend, and they are indeed the most wind-dominated and luminous sources in the luminosity-line-width plane.

4.3. Kinematically Unassociated Emission Lines in Several ERQs

We detect ERQs where the Balmer emission, [O III], and/or the C IV are significantly offset from each other in velocity space. We show the three sources in Figure 6. In SDSS J095823.14+500018.1, both C IV and H β are red-

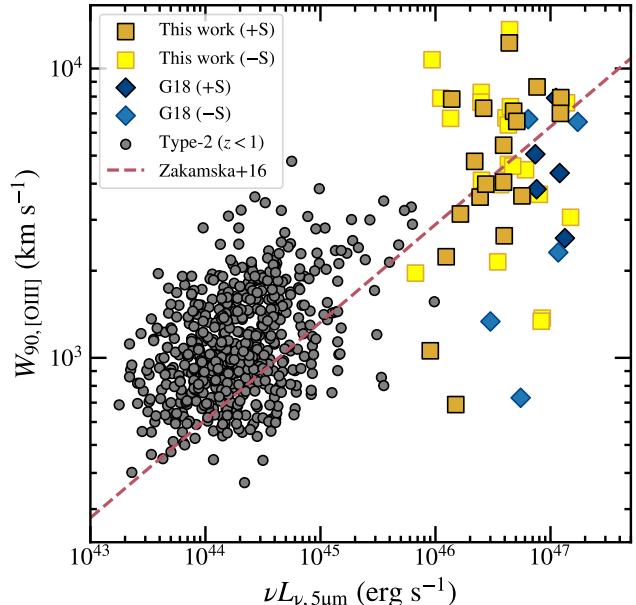


Figure 5. The W_{90} measurements of the [O III] λ 5008 line is plotted as a function of $5 \mu\text{m}$ luminosity for the ERQs as the yellow circles. The gray circles are the same measurements for obscured quasars at $z < 1$ from Zakamska & Greene (2014). In the legend, \pm S represent whether the sources’ $W_{90,[\text{OIII}]}$ is directly measured from the rest-frame optical spectra (+S) or inferred from $W_{90,\text{CIV}}$ (–S). The red dashed line is the relation obtained by Zakamska et al. (2016) for the type-2 quasars and ERQs.

shifted from [O III] by $\sim 2000 \text{ km s}^{-1}$. The C IV in SDSS J123241.73+091209.3 is blueshifted from the other two lines but matches a second peak near [O III] that cannot be accounted for by the weaker [O III] λ 4960 alone. In SDSS J155057.71+080652.1, the two kinematic components of C IV are each associated with [O III] and H β , while the latter two lines themselves are offset from each other by $\sim 2000 \text{ km s}^{-1}$. This hints at the presence of multiple unresolved sources or that the lines originate from spatially and kinematically different regions in the same source (e.g., Wylezalek et al. 2022; Vayner et al. 2023). More exotic explanations also include SMBH binaries or an off-nucleus recoiling SMBH retaining the BLR but leaving the NLR behind after being ejected in a BH merger event (e.g., Komossa 2012). We do not see significant C IV self-absorption features, which may also alter the emission line profile, in these sources.

4.4. ERQ X-ray Properties

In Figure 7, we show the intrinsic X-ray luminosity $L_{2-10 \text{ keV}}$ at rest-frame 2–10 keV as a function of mid-infrared luminosity $\nu L_{\nu,6\mu\text{m}}$ for both the ERQs and Hot-DOGs. Both populations are included in this figure for their similar SED properties as we outline in § 2.4.

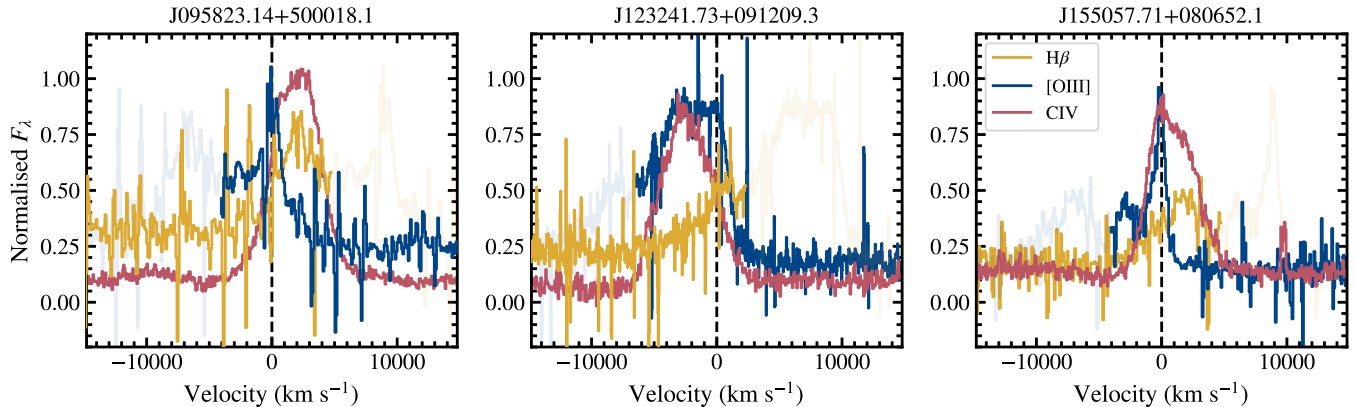


Figure 6. The $H\beta$, $[O\text{ III}]$, and $C\text{ IV}$ emission lines overplotted in velocity space in the rest-frame of $[O\text{ III}]\lambda 5008$ for the three ERQ targets showing signatures of extremely blueshifted NLR (or redshifted BLR) up to $\sim 2000\text{ km s}^{-1}$. The faint blue and yellow transparent traces are the full $H\beta+[O\text{ III}]$ profiles.

In total, 20 ERQ targets in our sample are detected in the full observed 0.3–7 keV energy band, and 20 ERQs are not detected. Similarly to previous X-ray studies on ERQs (Goulding et al. 2018; Ishikawa et al. 2021), we find that the HR-inferred gas column density of the X-ray-detected ERQs is consistent with sources being heavily obscured. Moreover, ~ 8 of these ERQs are approaching the Compton-thick regime of $N_{\text{H}} \geq 10^{24}\text{ cm}^{-2}$. Some of these Compton-thick sources are among the sources with the largest number of counts and thus the most luminous targets in our sample. All X-ray measurements on individual targets of our ERQ sample are listed in Table 3. Of course, as noted already by Goulding et al. (2018), N_{H} measurements from HR analysis are far less certain than those derived from X-ray spectra with far more counts. Nevertheless, hardness ratios with appropriate error bars still contain information of the energy spectrum of the sources. Unfortunately, none of our sources has sufficient counts to produce an X-ray spectrum to improve the N_{H} measurements, and only deeper X-ray observations in the future may help resolve this issue.

Visually inspecting the ERQs in the $L_{\text{X}} - L_{\text{MIR}}$ space, we find that X-ray-non-detected ERQs are concentrated at $\nu L_{\nu, 6\mu\text{m}} \gtrsim 4 \times 10^{46}\text{ erg s}^{-1}$. For the HotDOGs, only 3 out of the 18 targets are detected in 0.3–7 keV, and the others remain undetected. Given the similarity between ERQs and HotDOGs, we combine the two samples and divide them into 5 equal bins of MIR luminosity. Within each luminosity bin, we compute the X-ray detection fraction f_{X} and the associated 1σ uncertainties by maximizing a binomial likelihood

$$p(N_{\text{det}}|f_{\text{X}}, N) = \binom{N}{N_{\text{det}}} f_{\text{X}}^{N_{\text{det}}} (1 - f_{\text{X}})^{N - N_{\text{det}}}, \quad (4)$$

where N and N_{det} are the number of all sources and X-ray-detected sources, respectively. We find that the X-ray detection fraction overall drops as a function of MIR luminosity (upper panel of Figure 7).

Since our X-ray sample spans a range of exposure times, it is possible that the non-detections may simply be due to shallower exposure times. We thus scale the exposure times of all X-ray observations down to $\sim 4\text{ ks}$ – the minimum exposure time of our sample – and run the detection algorithm again. Roughly a third of the X-ray-detected sources become non-detected with this treatment, and we demonstrate in Figure 7 that the detection fraction still decreases as a function of MIR luminosity even with the simulated shorter exposure time for each target. Moreover, the mean redshifts of X-ray-non-detected and X-ray-detected ERQs are 2.64 and 2.59, respectively, and the source with the highest redshift ($z \approx 3.3$) yield a detection (Goulding et al. 2018). Thus, being higher redshift does not seem to preferentially result in non-detections in our sample. We conclude that the weakening of X-ray emission as a function of MIR luminosity is physical, as opposed to arising from a selection bias.

4.5. Average Properties of X-ray Non-detections

To harness the average X-ray properties of the undetected (or weakly detected) sources and to determine if they are intrinsically luminous in X-ray, we stack their *Chandra* images in the rest-frame 4–22 keV band with no weighting assigned to mimic the scenario where we would have observed one individual source over multiple pointings. We repeat the aperture photometry on the stacked image and detect a (stacked) source with total and net counts of 19 and 15.16, respectively (see inset of Figure 7). We also use BEHR to calculate $\text{HR}_2 = 0.01 \pm 0.26$ for the stacked detection. It is not obvious which

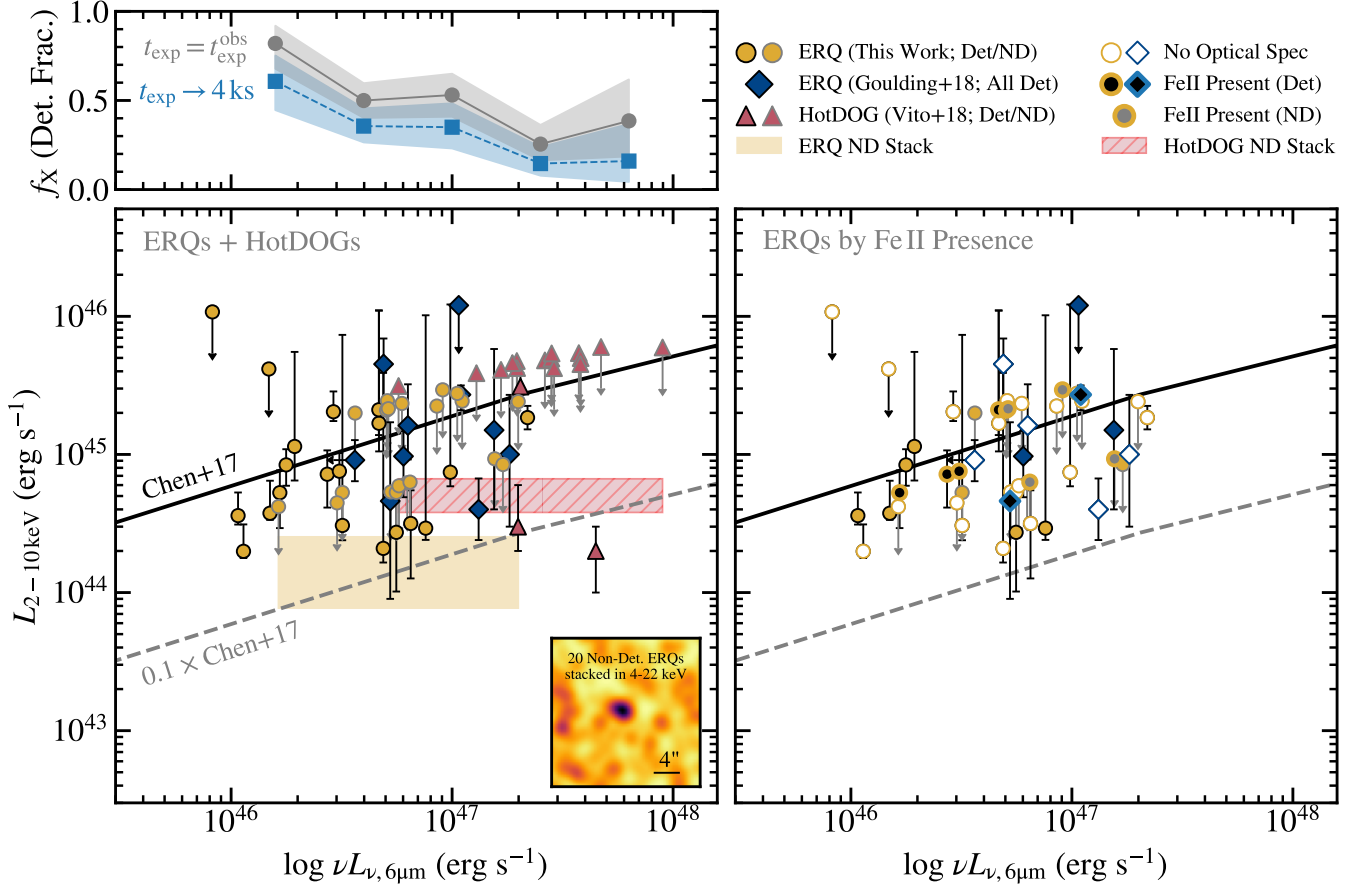


Figure 7. Lower Left: X-ray luminosity is plotted against the mid-infrared luminosity of ERQs and HotDOGs. Empty markers are observed luminosity and filled ones are the absorption-corrected X-ray luminosity. The filled yellow box represents our luminosity measurements from the X-ray-non-detected ERQ stacks, and the hatched red box represents the same measurement of Vito et al. (2018) done on the X-ray-non-detected HotDOGs, respectively. The stacked and smoothed image of the X-ray-non-detected ERQs in the rest-frame 4 – 22 keV band is shown as the inset, where the circle marks the aperture with which we conduct photometry. **Lower Right:** we label the ERQs with whether they have rest-frame optical spectra available (empty markers) and whether they have Fe II lines (black and gray fillings for X-ray-detected and -non-detected sources, respectively) in $L_X - L_{MIR}$ plane. In both panels, the X-ray non-detections are plotted as the 3σ upper limits of intrinsic L_X at $N_H = 10^{24} \text{ cm}^{-2}$. **Top Left:** The solid gray and dashed blue curves track detection fractions of both ERQs and HotDOGs in the observed 0.3–7 keV band as a function of $\nu L_{\nu,6\mu\text{m}}$ at the original exposure time and when all scaled down to ~ 4 ks, respectively; the shaded areas are the 1σ confidence intervals.

observing-cycle-dependent $N_H(z, \text{HR})$ interpolation we should use to compute N_H from this HR. However, the measured HR value of the stacked sources is consistent with $8 \times 10^{23} \text{ cm}^{-2} \lesssim N_H \lesssim 3 \times 10^{24} \text{ cm}^{-2}$ – this is 3–9 times denser than the median column density of $\langle N_H \rangle_{\text{det}} \approx 3 \times 10^{23} \text{ cm}^{-2}$ for the X-ray-detected sources. After accounting for the aforementioned range of N_H values and different observing cycles in PIMMS modelling and using the median redshift of the X-ray-non-detected ERQs, we estimate the intrinsic X-ray luminosity range to be $10^{43.9} \text{ erg s}^{-1} \lesssim L_{2-10 \text{ keV}} \lesssim 10^{44.4} \text{ erg s}^{-1}$, lower than the unreddened quasars for their $6 \mu\text{m}$ -luminosity range.

We also present the X-ray luminosity of the stacked X-ray-non-detected HotDOGs by Vito et al. (2018) along with our ERQ stack in Figure 7. Using HR analysis, we estimate the X-ray-non-detected HotDOGs to have $N_H = 1.4_{-0.9}^{+0.6} \times 10^{24} \text{ cm}^{-2}$, and the average intrinsic luminosity of the non-detected HotDOGs to be $\log L_{2-10 \text{ keV}} / \text{erg s}^{-1} = 44.5_{-0.3}^{+0.1}$ (see red hatched box in Figure 7) – both are consistent with Vito et al. (2018). Similar to the ERQs, the X-ray-non-detected HotDOGs are also heavily obscured and appear underluminous in X-ray for their MIR luminosities.

5. DISCUSSION

Using the X-ray observations of a large sample of MIR-selected very luminous quasars hosting extremely powerful outflows, we have found that the ERQ population is overall deficient in X-ray photons for their MIR luminosities. Certain ERQs also show particularly complex kinematic structures based on spectroscopic data. Here, we contextualize our findings, link the X-ray properties to the outflows, and ruminate on the possible implications of our results.

5.1. *The Missing X-ray Photons*

While many studies have found that unobscured blue quasars show a clear positive correlation between their MIR and X-ray luminosities (Gandhi et al. 2009; Stern 2015; Chen et al. 2017), a large fraction of the red quasars are X-ray non-detections with the detection fraction dropping at higher MIR luminosity (Figure 7). Goulding et al. (2018) find no X-ray weak ERQs but expect that this population may emerge in surveys with a more extensive search. Indeed, with the sample size now four times larger than the pilot study, we uncover the population of X-ray-weak ERQs.

One way to make an X-ray-non-detected ERQ is to obscure the source with a Compton-thick X-ray absorbing column. By stacking the X-ray images of the non-detections in the rest-frame 4–22 keV and making a significant detection at the source position (see §4.5 and the inset on the left panel of Figure 7), we show that there are indeed X-ray photons leaking out from these sources. This is suggestive of the presence of heavy obscuration at least in some sources with no significant X-ray detection. Such a claim would find support in the X-ray-detected ERQs, which are known to have nearly Compton-thick columns. Even more convincing, the inferred N_{H} of the non-detection stacks is 3 to 9 times higher than the average N_{H} of the X-ray-detected population, strongly pointing to the conclusion that the non-detections could be partially attributed to heavier obscurations in these systems. Analogously, both we and Vito et al. (2018) stack the images of the X-ray-non-detected HotDOGs and find that they have comparable gas column density to that of ERQs as well, providing additional circumstantial evidence for the obscuration picture given the similarity between the two populations.

However, the average intrinsic luminosity of the X-ray-non-detected ERQs is still ~ 0.5 –1 dex lower than that expected from the unobscured type-1 quasars of comparable MIR luminosity. Therefore, we suspect that, in addition to being heavily obscured, these non-detected ERQs may be intrinsically X-ray-weak as well. Besides the X-ray stacks, the fact that we find broad-line quasars

based on unambiguous detection of Fe II multiplet emission in the rest-frame optical provides a potential geometric argument to intrinsic X-ray weakness. Given the Fe II could be emitted as close to the black hole as ~ 0.01 –0.1 pc (Marinello et al. 2016), their presence in the spectra suggests that we may be looking directly at the BLR and possibly the corona with a less obscured line of sight. Therefore, the absence of X-ray emission seems more likely to arise from intrinsic weakness than obscuration. The five X-ray-non-detected ERQs with unambiguously detected Fe II emission are among such examples. Nonetheless, we still cannot rule out geometric effects, where the gas column only obscures the X-ray-emitting corona but not the entire broad-line region. Alternatively, ERQs may have more spatially extended broad-line regions than normal blue quasars.

In addition to the stacked sources, we also see some evidence of the combination of heavy obscuration and intrinsic X-ray weakness from the X-ray-detected ERQs. Goulding et al. (2018) find that ERQs show no deviation from the X-ray-to-infrared relations expected for unobscured type-1 quasars. However, with our extended sample, we see the X-ray-detected ERQs on average fall below the type-1 relations found by Stern (2015) and Chen et al. (2017) by a factor as much as ~ 5 or more (Figure 7). It is not unreasonable to argue that in addition to the measured nearly Compton-thick columns, intrinsic weakness is also responsible for the missing X-ray photons here. As the uncertainties on column densities could be as large as ~ 2 dex for some targets, it is possible that the luminosities of the X-ray-detected ERQs are spread evenly about the type-1 X-ray-to-infrared relations as well given the current measurement uncertainties. On the other hand, $L_{6\mu\text{m}}$ may be underestimated for the most obscured sources, making the X-rays even weaker for given MIR luminosity, relatively speaking.

5.2. *Linking X-ray Weakness with ERQ Outflows*

The natural question to ask next is what physical processes or environments could result in this combination of obscuration and intrinsic X-ray weakness that we observe in ERQs. Luckily, the outflow and winds that are ubiquitously found in this population may help solve the puzzle. Additionally, linking the outflows to the X-ray observations may shed light on the wind-launching mechanisms of the ERQs.

In Figure 8, we stack the $\text{H}\beta + [\text{O III}]$ complex for the X-ray-detected and non-detected ERQs and find that the non-detections show a significantly broader $[\text{O III}]$ profiles than the X-ray detections ($\Delta W_{90, [\text{O III}]} \approx 2000 - 3000 \text{ km s}^{-1}$). In the stacked C IV profiles shown in Figure 9, we see a qualitatively similar difference between

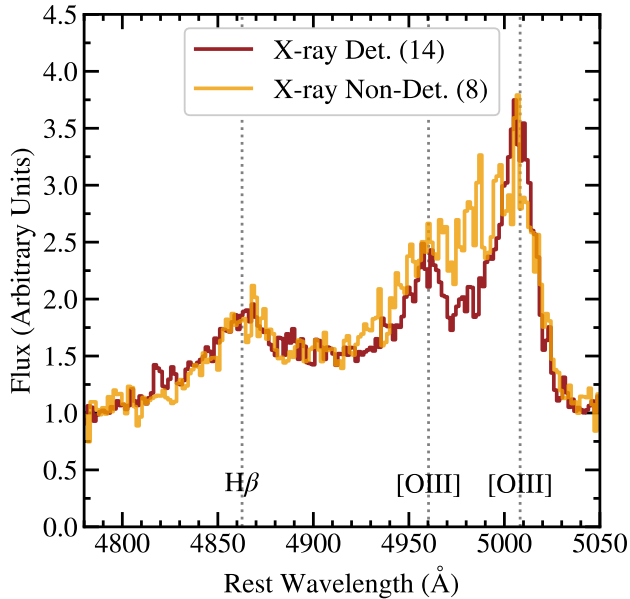


Figure 8. The stacked and normalized $H\beta+[O III]$ complex for the X-ray-detected and non-detected ERQ targets with rest-frame optical spectra available. J0854+1730 and J1102-0007 are excluded from the stack since their emission line complexes reside close to regions of significant telluric absorption.

the X-ray-detected and non-detected ERQ, although the relative broadening of the non-detections is much less significant than what we see in the $[O III]$ profile. This difference between the two emission lines may be due to geometric effects. Since the $C IV$ emission could be reprocessed by a thin layer of the dusty torus (Alexandroff et al. 2018; Zakamska & Alexandroff 2023), the bulk of the $C IV$ -emitting gas may be obscured. This obscuration picture can also be inferred in Figure 9, where the $Fe II$ -detected ERQs (less obscured) have a broader $C IV$ profile than the ERQs without $Fe II$ (more obscured). If this is indeed the case, the kinematics of $C IV$ reflects only a small portion of the gas covering angle over a small range of distances, whereas the $[O III]$ emission is sampled over larger distances and wider covering angles, thus being a better tracer of the quasars’ capability to launch winds/outflows.

Although we have treated the non-detections separately, we do not think X-ray detection divides the ERQs into two physically distinct groups. Rather, the difference in the line widths of the X-ray-detected and -non-detected ERQs could help us infer the wind-launching mechanism of the entire ERQ population. The correlation between X-ray weakness and strong outflow has always been expected for line-driven winds, a popular mechanism for launching quasar outflows (Shlosman

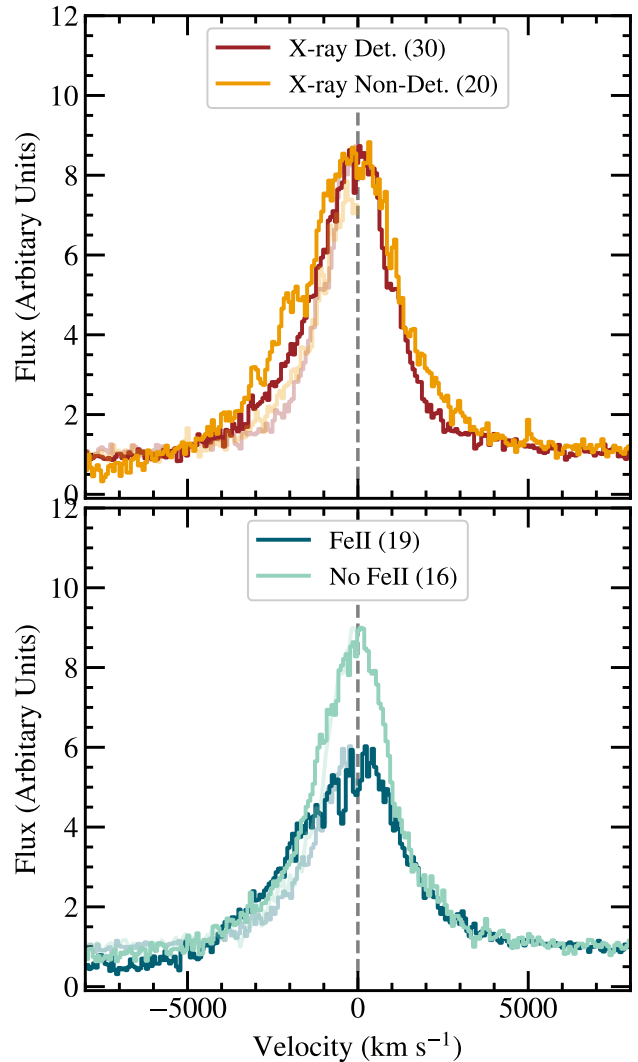


Figure 9. Upper Panel: Stacked and normalized $C IV$ profiles by X-ray detection. **Lower Panel:** Stacked and normalized $C IV$ profiles by the presence of $Fe II$ lines in the rest-frame optical spectra. In both panels, the lighter traces at $v < 0 \text{ km s}^{-1}$ are the reflections of spectra at $v > 0 \text{ km s}^{-1}$ to show the asymmetry of line profiles. The numbers in the legends are the number of individual spectra stacked in each case.

et al. 1985; Murray et al. 1995). In large surveys of active galactic nucleus outflows, outflow velocities are overall positively correlated with the bolometric luminosities of the active galactic nuclei (e.g., Zakamska & Greene 2014; Leung et al. 2019) – naïvely, one would think stronger X-ray emission should be associated with stronger outflow activity. Yet, quasars with the strongest outflow such as BALs (e.g., Luo et al. 2014; Lusso et al. 2021, 2023) and some HotDOGs (e.g., Ricci et al. 2017; Vito et al. 2018) tend to be associated with intrinsic X-ray weakness. Theoretical work demonstrates that powerful

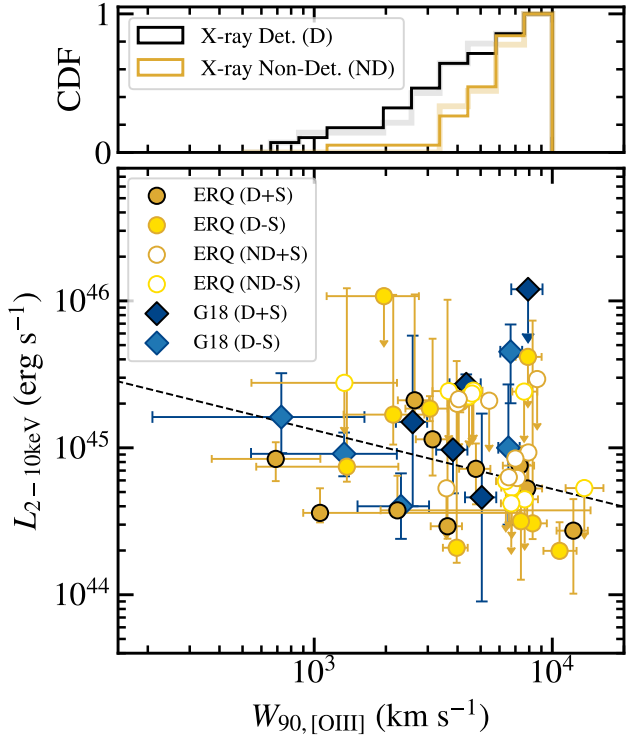


Figure 10. Upper Panel: The more opaque cumulative histogram of [O III] line widths for all the X-ray-detected (D) and -non-detected (ND) ERQs. The lighter histograms are produced only using ERQs with rest-frame optical spectra available. **Lower Panel:** The intrinsic X-ray luminosity of the ERQs is plotted as a function of [O III] line width.

circumnuclear winds can be launched when the gas near the accretion disk absorbs the quasar’s UV photons and gets accelerated as a result (Proga et al. 1999, 2000). However, this can only occur if the gas is in the proper ionization state to have high bound-bound opacity. An overabundance of X-ray photons at a high enough accretion rate (and thus bolometric luminosity) could overionize the circumnuclear medium, decrease gas opacity, and thus disable the central engine from radiatively launching strong outflows (Proga et al. 2000; Proga & Kallman 2004).

With this picture in mind, we may explain the observed correlation between X-ray weakness and strong outflow activity. Since [O III] is not line-driven (e.g. Dopita et al. 2002), it is plausible that the [O III]-emitting gas is accelerated by the line-driven wind closer to the nuclear region with some yet-to-be-identified coupling mechanisms between the two gas phases. It is also possible that the fast-[O III] outflows are driven by radiation pressure on dust (Keating et al. 2012; Thompson et al. 2015; Ishibashi et al. 2018), which has been claimed to be a common feedback mechanism particularly in lu-

minous red quasar populations (Ishibashi et al. 2017). However, this mechanism does not necessarily require intrinsic X-ray weakness.

Aside from the emission line stacks (Figure 8 and 9), we demonstrate in Figure 10 that the X-ray luminosities of the X-ray-detected ERQs may show a negative correlation with [O III] line width with a Spearman correlation factor of $r_s = -0.39$ and $p = 0.03$. While the p-value is marginal, still this correlation is suggestive, and it is a high priority to confirm with more rest-frame optical spectra. The cumulative distribution function (CDF) of the [O III] line widths for the X-ray non-detections is also preferentially located at higher $W_{90,[OIII]}$ values when compared with that for the X-ray-detected ERQs. In Figure 10, the preference for weaker outflows at higher L_X is even more obvious in the CDFs produced only using ERQs with directly measured $W_{90,[OIII]}$ and excluding those calibrated from CIV. Both panels of Figure 10 point towards a potential causal relationship between X-ray weakness and the presence of strong outflow.

5.3. Are ERQs Super-Eddington Accretors?

Given their high bolometric luminosities ($L_{bol} \approx 10^{47-48} \text{ erg s}^{-1}$) inferred from MIR luminosities and fast outflows, ERQs are considered to be potential sites of near- or super-Eddington accretions with $L/L_{Edd} \approx 0.5 - 10$ at Cosmic Noon (Zakamska et al. 2016, 2019; Perrotta et al. 2019). Such an assumption may also offer explanations for the observed X-ray weakness in ERQs. At high Eddington ratios, the accretion disk could launch a disk wind into the hot corona. The wind can then Compton-cool the corona by introducing softer photons and thus quenching its ability to up-scatter UV photons into X-ray (Proga 2005). Moreover, it is also possible that the disk wind is so optically thick that it shields the corona and starves it from receiving the seed UV photons to be up-scattered, consequently suppressing the X-ray emission and making an intrinsically X-ray weak quasar. In part, this latter scenario seems to resonate with the high obscuration, and particularly the X-ray-non-detected ERQs.

Moreover, Jiang et al. (2019) perform global three-dimensional radiation magnetohydrodynamical simulations of super-Eddington accretion onto SMBHs and show that at such high accretion rates, the accretion disk becomes optically thick enough that the accretion power is thermalized due to efficient cooling. If angular momentum in these disks is transported by spiral shocks, sufficient hot gas does not exist to up-scatter the photons in the simulation, consequently making the quasar weak in X-ray. When invoking magnetorotational instability to transport angular momentum in the simulation,

hot gas can be produced, but optically thick winds are launched from the super-Eddington disks and obscure the X-ray emitting regions for most observing angles, also resulting in an apparent X-ray weak quasar. However, we note that in this case, the wind is continuum-driven instead of line-driven, as the latter becomes inefficient in the optically thick regime (e.g., Castor et al. 1975; Gräfenor et al. 2017). In this case, the broader [O III] profile may reflect the higher accretion luminosity of these X-ray-non-detected and potentially super-Eddington ERQs; the less significant broadening of C IV with respect to X-ray detections may be a result of obscuration and/or the fact that the line-driven mechanism is irrelevant in this scenario.

5.4. Complications From the Wider Environment

Up until now, our analysis and discussion assume that each system only has a single black hole in a single galaxy host, but there is the possibility that the high luminosities and complicated line morphologies in both rest-frame optical and UV may be due to multiple objects along the line of sight in some cases. Indeed, galaxy mergers could cause the broad forbidden lines in the ERQs, but Zakamska et al. (2019) find no obvious companions for $\sim 8 - 9$ out of 10 selected ERQ targets based on imaging data from *Hubble Space Telescope* (*HST*). With *JWST*, Wylezalek et al. (2022) find SDSS J165202.64+172852.3 – the one source with *HST*-detected companions – to be a red quasar living in an extremely dense and dynamic protocluster environment, with multiple companion galaxies present on scales of ~ 10 kpc. Thus, in addition to the ubiquitous powerful outflows found in ERQs, unresolved companions and other velocity components in a merger environment may also contribute to the total luminosity and line width of the blended optical emission lines.

The three sources we show in Figure 6 may also support the clustering scenario. For example, the coincidental match-up of the H β and [O III] with the two components of C IV line in SDSS J155057.71+080652.1 hints at the presence of multiple unresolved companion sources. Although the typical velocity of galaxies in a clustering environment is $600 - 1000 \text{ km s}^{-1}$, projected velocities as high as $\sim 2000 \text{ km s}^{-1}$ potentially due to clustering has been observed as well (Heckman et al. 2009). Moreover, Wylezalek et al. (2022) point out that the protoclusters may not be virialized yet at $z = 2 - 3$, so producing such line kinematics is not impossible. Even if in fact there is no companion interaction, such observations may also be used to probe the kinematics and structures of different line-emitting regions in the quasar’s immediate environment and outflow. The explanations for the significantly

kinematically unassociated C IV, [O III], and/or H β we mentioned in § 4.2, such as recoiling SMBHs or SMBH binaries, all invoke dynamical effects likely introduced by past and/or ongoing merger activity as well.

Nonetheless, future spatially resolved spectroscopic observations with *JWST*, which have already been proven successful in at least one ERQ system (Wylezalek et al. 2022) thanks to the instrument’s high angular resolution, would be crucial to studying these ERQ targets. Such observations will help one better constrain the geometry and spatial distribution of the outflowing, X-ray-obscuring material and potential companions in the hosts’ immediate environment. With a more extensive survey, one can test whether the protocluster environment would be able to explain the unusually large line widths and other properties of the ERQs (Wylezalek et al. 2022) when compared with blue quasars. It could also offer a possibility to test the more exotic hypotheses on the origins of the kinematically unassociated emission lines in certain ERQ targets.

6. CONCLUSION

We present an extensive X-ray study of a total of 50 extremely red quasars at $z = 2 - 3$ selected by their broad C IV $\lambda 1549$ line width with proposed *Chandra* observation and archival data. The X-ray data is also supplemented with a spectroscopic sample of 35 ERQs whose rest-frame optical spectra are obtained either from Magellan/FIRE follow-up observations or by Perrotta et al. (2019). A total of 24 objects in the spectroscopic sample overlap with the X-ray sources. In this work, we attempt to link the X-ray emission to the powerful outflows ubiquitously found in these quasars by combining ground-based spectroscopic observations with the X-ray data. We summarize the main findings of our analysis as follows.

To measure the width of the [O III] $\lambda 5008$ line and quantify the outflow activity, we perform multi-Gaussian fits of the H β + [O III] complex of the ERQs with available rest-frame optical spectra using a maximum of three components representing the NLR, BLR, and outflows. We find that many ERQs show BLR emission in the rest-frame optical, including the Fe II multiplet pseudo-continuum and broad and symmetric Balmer emissions. We also conduct multicomponent fits on the C IV $\lambda 1549$ emission lines of the ERQs, obtain a line width relation between the C IV and [O III], and approximate the [O III] line widths for the ERQs without rest-frame optical spectra; nonetheless, it is always the rest-frame optical spectra that would provide the most reliable line width measurements. All direct [O III] line width measurements except for two sources are higher

than 2000 km s^{-1} , strongly suggesting the presence of powerful outflow.

On the X-ray end, our analysis reveals a population of previously unknown X-ray-non-detected ERQs. The X-ray detection fraction drops as a function of MIR luminosity. We interpret that such X-ray weakness could be due to heavy obscuration, given that we estimate the average gas column density of the X-ray-non-detected ERQs to be $\gtrsim 10^{24} \text{ cm}^{-2}$ and higher than that of the X-ray-detected ERQs. Additionally, we infer that the ERQs also must be intrinsically weak in X-ray since the intrinsic X-ray luminosities of both the detected ERQs (on average) and the stacked non-detections reside below the $L_X - L_{\text{MIR}}$ relation for unobscured type-1 quasars. The presence of type-1 spectral features found in the rest-frame optical spectra of the non-detected ERQs may also be indirect evidence of intrinsic X-ray weakness.

Moreover, we find that the X-ray-non-detected ERQs tend to launch more powerful [O III]-emitting outflows than the X-ray-detected ones do. One option to explain such correlation is that the strong line-driven winds launched at smaller scales, which require intrinsic X-ray weakness, are then coupled with and (potentially mechanically) accelerate the observed [O III]-emitting gas to kpc-scales. Another option is that ERQs are indeed super-Eddington accretors. In this scenario, numerical

simulations suggest that such quasars are naturally X-ray weak (Jiang et al. 2019). The larger line widths for the non-detections are due to their higher accretion luminosities, resulting in more powerful continuum-driven winds in the circumnuclear region that subsequently accelerate gas to large scales.

Lastly, the environments in which ERQs reside may also be complicated. Our spectral fitting reveals that some ERQs show large velocity offset between BLR and NLR emission lines that likely cannot be accounted for with a single SMBH. Protocluster environments, binary SMBHs, or gravitational recoils from SMBH mergers could be invoked to explain such line kinematics. Future spatially resolved spectroscopic observations by *JWST* are required to further study the environmental effect on this quasar population.

ACKNOWLEDGEMENTS

We thank the anonymous referee for the detailed report that leads to improvement of this manuscript. We also acknowledge the support of the grant NSF AAG AWD1007094. This paper employs a list of *Chandra* datasets, obtained by the *Chandra X-ray Observatory*, contained in the Chandra Data Collection 261 (doi:10.25574/cdc.261). YM is also grateful for Shengfan Cao’s help and suggestions in optimizing the spectral fitting procedures used in this work.

Table 1. X-ray Sample of Extremely Red Quasars

Target	ObsID	RA	Dec	z	FWHM(C IV) [km s^{-1}]	$\log \nu L_{\nu, 6\mu\text{m}}$ [erg s^{-1}]	[O III] spec?
(1)	(2)	(3)	(4)	(5)	(6)	(7)	(8)
SDSS J0024+2450	CXO20762	00:24:00.25	+24:50:31.9	2.7859	3523 ± 195	47.05 ± 0.04	×
SDSS J0047+2640	CXO23748	00:47:13.21	+26:40:24.7	2.5412	3685 ± 74	46.72 ± 0.05	×
SDSS J0050-0212	CXO23749	00:50:44.95	-02:12:17.6	2.2430	4343 ± 487	46.17 ± 0.06	×
SDSS J0116-0505	CXO18210	01:16:01.43	-05:05:03.9	3.1784	2291 ± 253	47.34 ± 0.03	×
SDSS J0152+3231	CXO20766	01:52:22.58	+32:31:52.7	2.7803	3677 ± 104	46.71 ± 0.04	×
SDSS J0805+4541	CXO20758	08:05:47.66	+45:41:59.0	2.2992	2667 ± 107	46.70 ± 0.03	✓
SDSS J0826+5653	CXO23750	08:26:18.04	+56:53:45.9	2.3452	3509 ± 135	46.22 ± 0.06	✓
SDSS J0826+1639	CXO23571,24930	08:26:49.30	+16:39:45.2	2.3111	5633 ± 150	46.03 ± 0.07	✓
SDSS J0854+1730	CXO23752	08:54:51.11	+17:30:09.1	2.6029	4199 ± 207	46.50 ± 0.06	✓
SDSS J0958+5000	CXO23753	09:58:23.15	+50:00:17.7	2.3376	4345 ± 32	46.75 ± 0.03	✓
SDSS J1013+3427	CXO20755	10:13:24.53	+34:27:02.6	2.4582	4157 ± 51	46.88 ± 0.03	✓
SDSS J1021+2144	CXO23754	10:21:30.74	+21:44:38.4	2.1968	3567 ± 92	46.18 ± 0.08	✓
SDSS J1025+2454	CXO23755	10:25:41.78	+24:54:24.2	2.4095	5324 ± 64	47.19 ± 0.01	✓

Table 1 continued

Table 1 (*continued*)

Target	ObsID	RA	Dec	z	FWHM(C IV) [km s ⁻¹]	$\log \nu L_{\nu, 6\mu\text{m}}$ [erg s ⁻¹]	[O III] spec?
(1)	(2)	(3)	(4)	(5)	(6)	(7)	(8)
SDSS J1034+1430	CXO23756	10:34:56.95	+14:30:12.5	2.9560	5949 ± 367	46.75 ± 0.07	×
SDSS J1046+0243	CXO20754	10:46:11.50	+02:43:51.6	2.7702	4854 ± 126	47.30 ± 0.03	×
SDSS J1047+4844	CXO20763	10:47:18.35	+48:44:33.8	2.2747	2521 ± 51	46.67 ± 0.03	×
SDSS J1047+6213	CXO23757	10:47:54.59	+62:13:00.2	2.5398	5081 ± 133	46.50 ± 0.06	×
SDSS J1102-0007	CXO23758	11:02:02.68	-00:07:52.7	2.6174	3767 ± 282	46.25 ± 0.07	✓
SDSS J1117+4623	CXO20759	11:17:29.56	+46:23:31.2	2.1282	3053 ± 54	46.46 ± 0.04	×
SDSS J1138+4732	CXO20767	11:38:34.68	+47:32:50.0	2.3169	3296 ± 104	46.56 ± 0.04	✓
SDSS J1217+0234	CXO20756	12:17:04.70	+02:34:17.1	2.4268	2604 ± 55	46.67 ± 0.04	✓
SDSS J1232+0912	CXO23759	12:32:41.73	+09:12:09.3	2.3906	4787 ± 52	47.23 ± 0.02	✓
SDSS J1254+2104	CXO20757	12:54:49.50	+21:04:48.4	3.1145	2482 ± 48	46.99 ± 0.03	×
SDSS J1307+3648	CXO11572	13:07:41.38	+36:48:43.0	2.3375	3633 ± 97	46.06 ± 0.07	×
SDSS J1309+5601	CXO20760	13:09:36.14	+56:01:11.3	2.5730	3630 ± 114	46.93 ± 0.03	×
SDSS J1342+6056	CXO23760	13:42:48.86	+60:56:41.1	2.4127	2652 ± 102	45.92 ± 0.07	×
SDSS J1344+4454	CXO20761	13:44:17.34	+44:54:59.4	3.0301	2871 ± 70	47.02 ± 0.03	×
SDSS J1344+1401	CXO23761	13:44:50.51	+14:01:39.2	2.7318	4487 ± 191	46.48 ± 0.06	×
SDSS J1345+6000	CXO23762	13:45:35.66	+60:00:28.4	2.9253	6460 ± 742	46.69 ± 0.06	×
SDSS J1348-0250	CXO23763	13:48:00.13	-02:50:06.4	2.2261	3654 ± 151	46.44 ± 0.04	✓
SDSS J1355+1447	CXO20765	13:55:57.60	+14:47:33.1	2.6852	2958 ± 60	46.77 ± 0.03	×
SDSS J1456+2145	CXO23764	14:56:23.35	+21:45:16.2	2.4642	4422 ± 148	46.49 ± 0.03	✓
SDSS J1501+2317	CXO23765	15:01:17.07	+23:17:30.9	3.0169	4035 ± 130	46.80 ± 0.05	✓
SDSS J1531+1058	CXO23767	15:31:07.14	+10:58:25.8	2.7822	3937 ± 146	46.76 ± 0.05	×
SDSS J1542+1020	CXO20764	15:42:43.87	+10:20:01.5	3.2025	3901 ± 286	46.96 ± 0.04	✓
SDSS J1550+0806	CXO23766	15:50:57.71	+08:06:52.1	2.4868	4446 ± 60	46.29 ± 0.07	✓
SDSS J1604+5633	CXO20768	16:04:31.55	+56:33:54.2	2.4925	4221 ± 82	46.71 ± 0.02	✓
SDSS J1714+4148	CXO23768	17:14:20.38	+41:48:15.7	2.3220	3816 ± 109	46.21 ± 0.06	×
SDSS J2254+2327	CXO23769	22:54:38.30	+23:27:14.5	3.0838	4412 ± 146	46.81 ± 0.12	×
SDSS J2323-0100	CXO23770	23:23:26.17	-01:00:33.1	2.3724	3989 ± 62	46.81 ± 0.03	✓
SDSS J0006+1215 ^G	XMM763780701	00:06:10.67	+12:15:01.2	2.309	3523 ± 195	47.16 ± 0.01 (47.04)	✓
SDSS J0220+0137 ^G	CXO18708	02:20:52.13	+01:37:11.4	3.318	3685 ± 74	47.43 ± 0.04 (47.26)	×
SDSS J0826+0542 ^G	CXO18206	08:26:53.42	+05:42:47.3	2.578	4343 ± 487	47.00 ± 0.04 (46.78)	✓
SDSS J0832+1615 ^G	CXO18207	08:32:00.20	+16:15:00.3	2.431	2291 ± 253	47.00 ± 0.03 (46.72)	✓
SDSS J0834+0159 ^G	XMM762260101	08:34:48.48	+01:59:21.1	2.591	3677 ± 104	47.23 ± 0.03 (47.03)	✓
SDSS J0915+5613 ^G	CXO04821	09:15:08.45	+56:13:16.0	2.857	2667 ± 107	46.97 ± 0.05 (46.69)	×
SDSS J1121+5705 ^G	CXO06958	11:21:24.55	+57:05:29.6	2.383	3509 ± 135	46.79 ± 0.02 (46.80)	×
SDSS J1310+3225 ^G	XMM020540401	13:10:47.78	+32:25:18.3	3.009	5633 ± 150	47.15 ± 0.02 (47.12)	×
SDSS J1652+1728 ^G	CXO18205	16:52:02.64	+17:28:52.4	2.942	4199 ± 207	47.22 ± 0.02 (47.19)	✓
SDSS J2129-0018 ^G	XMM729160501	21:29:51.40	-00:18:04.3	3.206	4345 ± 32	< 46.54 (< 46.56)	×

Table 1 *continued*

Table 1 (*continued*)

Target	ObsID	RA	Dec	z	FWHM(C IV)	$\log \nu L_{\nu, 6\mu\text{m}}$	[O III] spec?
					[km s ⁻¹]	[erg s ⁻¹]	
(1)	(2)	(3)	(4)	(5)	(6)	(7)	(8)

NOTE—(1) The target name in the SDSS HHMM±DDMM format. (2) ObsID. (3)–(4) J2000 coordinates. (5) Redshift. (6) Full-width-half-maximum of the C IV λ 1549 emission line. (7) The 6 μm -luminosities measured by power-law interpolation on *WISE* photometry; the parenthesized values are measured by [Goulding et al. \(2018\)](#); on average, the 6 μm -luminosity is ~ 1.3 times larger than the 5 μm -luminosity. (8) Does the target have rest-frame optical spectrum available?

NOTE—Targets with a superscript “G” are sources studied by [Goulding et al. \(2018\)](#).

Table 2. Line Width Measurements of Extremely Red Quasars

Target	$W_{90, \text{CIV}}$	$W_{90, [\text{OIII}]}$	Broad Balmer?	Fe II?	Where [O III]
	[km s ⁻¹]	[km s ⁻¹]			
(1)	(2)	(3)	(4)	(5)	(6)
SDSS J082649.30+163945.2	8773 ⁺¹³¹⁶ ₋₁₃₁₆	1058 ⁺⁶²³⁵ ₋₁₅₉	✓	×	FIRE
SDSS J085451.11+173009.1	6278 ⁺⁹⁴² ₋₉₄₂	3594 ⁺⁵³⁹ ₋₅₃₉	×	×	FIRE
SDSS J102130.74+214438.4	4606 ⁺⁶⁹¹ ₋₆₉₁	2236 ⁺¹²²⁴² ₋₃₃₅	✓	×	FIRE
SDSS J110202.68–000752.7	13015 ⁺²¹⁴⁸ ₋₁₉₅₂	689 ⁺³⁷² ₋₃₁₈	✓	×	FIRE
SDSS J145623.35+214516.2	6547 ⁺⁹⁸² ₋₉₈₂	7292 ⁺¹⁰⁹⁴ ₋₁₀₉₄	✓	✓	FIRE
SDSS J150117.07+231730.9	6026 ⁺⁹⁰⁴ ₋₉₀₄	7117 ⁺¹⁰⁶⁷ ₋₁₀₆₇	×	×	FIRE
SDSS J154243.87+102001.5	6272 ⁺⁹⁴¹ ₋₉₄₁	8637 ⁺⁴²¹¹ ₋₁₂₉₆	✓	✓	FIRE
SDSS J000610.67+121501.2	6132 ⁺²²⁸⁷ ₋₉₂₀	4352 ⁺⁶⁵³ ₋₆₅₃	✓	✓	P19
SDSS J001120.22+260109.2	5637 ⁺⁸⁴⁶ ₋₈₄₆	7231 ⁺¹⁰⁸⁵ ₋₁₀₈₅	✓	✓	P19
SDSS J013413.22–023409.7	9111 ⁺¹⁷⁸⁸ ₋₁₃₆₇	16512 ⁺²⁴⁷⁷ ₋₂₄₇₇	✓	✓	P19
SDSS J020932.15+312202.7	4001 ⁺⁶⁰⁰ ₋₆₀₀	2403 ⁺³⁶⁰ ₋₃₆₀	×	×	P19
SDSS J080547.66+454159.0	5581 ⁺¹³⁵⁸ ₋₈₃₇	5431 ⁺⁸¹⁵ ₋₈₁₅	✓	✓	P19
SDSS J082618.04+565345.9	6313 ⁺⁹⁴⁷ ₋₉₄₇	7841 ⁺¹²¹⁹ ₋₁₁₇₆	✓	✓	P19
SDSS J082653.42+054247.3	3684 ⁺⁵⁵³ ₋₅₅₃	3827 ⁺⁵⁷⁴ ₋₅₇₄	×	×	P19
SDSS J083200.20+161500.3	5948 ⁺⁹⁷⁶ ₋₈₉₂	5057 ⁺⁷⁵⁹ ₋₇₅₉	✓	✓	P19
SDSS J083448.48+015921.1	4490 ⁺⁶⁷³ ₋₆₇₃	7911 ⁺¹¹⁸⁷ ₋₁₁₈₇	✓	×	P19
SDSS J091303.90+234435.2	3928 ⁺⁵⁸⁹ ₋₅₈₉	2611 ⁺³⁹² ₋₃₉₂	×	×	P19
SDSS J093226.93+461442.8	3861 ⁺⁹³⁷ ₋₅₇₉	3814 ⁺⁵⁷² ₋₅₇₂	×	×	P19
SDSS J095823.14+500018.1	5595 ⁺⁸³⁹ ₋₈₃₉	12262 ⁺¹⁸³⁹ ₋₁₈₃₉	✓	×	P19
SDSS J101324.53+342702.6	6709 ⁺¹⁰⁰⁶ ₋₁₀₀₆	3630 ⁺⁵⁴⁴ ₋₅₄₄	✓	×	P19
SDSS J102541.78+245424.2	6798 ⁺¹²⁰¹ ₋₁₀₂₀	7932 ⁺¹¹⁹⁰ ₋₁₁₉₀	✓	✓	P19
SDSS J103146.53+290324.1	5864 ⁺⁸⁸⁰ ₋₈₈₀	5508 ⁺²²³⁴ ₋₁₆₃₈	✓	✓	P19
SDSS J113834.68+473250.0	5255 ⁺⁷⁸⁸ ₋₇₈₈	3985 ⁺⁵⁹⁸ ₋₅₉₈	✓	×	P19
SDSS J121704.70+023417.1	3601 ⁺⁵⁴⁰ ₋₅₄₀	2641 ⁺³⁹⁶ ₋₃₉₆	✓	✓	P19

Table 2 *continued*

Table 2 (continued)

Target	$W_{90,\text{CIV}}$ [km s ⁻¹]	$W_{90,[\text{OIII}]}$ [km s ⁻¹]	Broad Balmer?	Fe II?	Where [O III]
(1)	(2)	(3)	(4)	(5)	(6)
SDSS J123241.73+091209.3	6262 ⁺⁹³⁹ ₋₉₃₉	6997 ⁺¹⁰⁵⁰ ₋₁₀₅₀	✓	×	P19
SDSS J134254.45+093059.3	4289 ⁺⁶⁴³ ₋₆₄₃	5734 ⁺⁸⁶⁰ ₋₈₆₀	✓	✓	P19
SDSS J134800.13-025006.4	5282 ⁺⁴³²⁸ ₋₇₉₂	4777 ⁺⁷¹⁷ ₋₇₁₇	✓	✓	P19
SDSS J135608.32+073017.2	3374 ⁺¹⁷¹⁷ ₋₅₀₆	2421 ⁺⁴¹⁷ ₋₃₈₆	✓	×	P19
SDSS J155057.71+080652.1	5325 ⁺⁷⁹⁹ ₋₇₉₉	3142 ⁺⁴⁷¹ ₋₄₇₁	✓	×	P19
SDSS J160431.55+563354.2	6574 ⁺⁹⁸⁶ ₋₉₈₆	4046 ⁺⁶⁰⁷ ₋₆₀₇	✓	✓	P19
SDSS J165202.64+172852.3	4171 ⁺⁶²⁶ ₋₆₂₆	2592 ⁺³⁸⁹ ₋₃₈₉	✓	×	P19
SDSS J215855.10-014717.9	7692 ⁺¹¹⁵⁴ ₋₁₁₅₄	9545 ⁺¹⁴³² ₋₁₄₃₂	✓	✓	P19
SDSS J221524.00-005643.8	5510 ⁺⁸²⁶ ₋₈₂₆	4010 ⁺⁶⁰² ₋₆₀₂	✓	✓	P19
SDSS J232326.17-010033.1	5302 ⁺⁷⁹⁵ ₋₇₉₅	6566 ⁺⁹⁸⁵ ₋₉₈₅	✓	✓	P19
SDSS J232611.97+244905.7	3717 ⁺⁵⁷¹ ₋₅₅₈	2741 ⁺⁴¹¹ ₋₄₁₁	✓	✓	P19
SDSS J002400.25+245031.9	4504 ⁺⁶⁷⁶ ₋₆₇₆	3673 ⁺⁴⁷⁶ ₋₅₃₆	C IV-calibrated
SDSS J004713.21+264024.7	5962 ⁺⁸⁹⁴ ₋₈₉₄	6754 ⁺⁸⁰⁷ ₋₆₄₇	C IV-calibrated
SDSS J005044.95-021217.6	6504 ⁺⁹⁷⁶ ₋₉₇₆	7901 ⁺¹¹¹⁸ ₋₈₈₅	C IV-calibrated
SDSS J011601.43-050503.9	4220 ⁺⁶³³ ₋₆₃₃	3060 ⁺⁵⁷⁶ ₋₆₄₄	C IV-calibrated
SDSS J015222.58+323152.7	4969 ⁺⁷⁴⁵ ₋₇₄₅	4662 ⁺⁴²⁸ ₋₄₃₁	C IV-calibrated
SDSS J022052.13+013711.4	5861 ⁺⁸⁷⁹ ₋₈₇₉	6540 ⁺⁷⁵⁴ ₋₆₀₈	C IV-calibrated
SDSS J091508.45+561316.0	5928 ⁺⁸⁸⁹ ₋₈₈₉	6682 ⁺⁷⁸⁹ ₋₆₃₄	C IV-calibrated
SDSS J103456.95+143012.5	9199 ⁺¹³⁸⁰ ₋₁₃₈₀	13627 ⁺²⁷⁷⁰ ₋₂₂₅₁	C IV-calibrated
SDSS J104611.50+024351.6	6369 ⁺⁹⁵⁵ ₋₉₅₅	7613 ⁺¹⁰³⁹ ₋₈₂₁	C IV-calibrated
SDSS J104718.35+484433.8	3783 ⁺⁵⁶⁷ ₋₅₆₇	2147 ⁺⁷⁵⁴ ₋₈₁₉	C IV-calibrated
SDSS J104754.59+621300.2	6677 ⁺¹⁰⁰² ₋₁₀₀₂	8268 ⁺¹²¹⁸ ₋₉₇₁	C IV-calibrated
SDSS J111729.56+462331.2	4708 ⁺⁷⁰⁶ ₋₇₀₆	4107 ⁺⁴³⁸ ₋₄₇₅	C IV-calibrated
SDSS J112124.56+570529.3	2461 ⁺³⁶⁹ ₋₃₆₉	728 ⁺⁸⁹⁸ ₋₅₁₈	C IV-calibrated
SDSS J125449.50+210448.4	3342 ⁺⁵⁰¹ ₋₅₀₁	1371 ⁺⁸⁸⁵ ₋₈₀₀	C IV-calibrated
SDSS J130741.38+364843.0	7835 ⁺¹¹⁷⁵ ₋₁₁₇₅	10727 ⁺¹⁹¹⁶ ₋₁₅₄₇	C IV-calibrated
SDSS J130936.14+560111.3	4878 ⁺⁷³² ₋₇₃₂	4469 ⁺⁴²⁴ ₋₄₄₀	C IV-calibrated
SDSS J131047.78+322518.3	3866 ⁺⁵⁸⁰ ₋₅₈₀	2314 ⁺⁷²² ₋₇₉₄	C IV-calibrated
SDSS J134248.86+605641.1	3690 ⁺⁵⁵³ ₋₅₅₃	1963 ⁺⁷⁸⁹ ₋₈₃₅	C IV-calibrated
SDSS J134417.34+445459.4	3318 ⁺⁴⁹⁸ ₋₄₉₈	1339 ⁺⁸⁸⁸ ₋₇₉₄	C IV-calibrated
SDSS J134450.51+140139.2	6388 ⁺²²³² ₋₉₅₈	7655 ⁺¹⁰⁵⁰ ₋₈₃₁	C IV-calibrated
SDSS J134535.66+600028.4	4642 ⁺⁶⁹⁶ ₋₆₉₆	3967 ⁺⁴⁴⁶ ₋₄₉₅	C IV-calibrated
SDSS J135557.60+144733.1	4941 ⁺⁷⁴¹ ₋₇₄₁	4602 ⁺⁴²⁶ ₋₄₃₄	C IV-calibrated
SDSS J153107.14+105825.8	5788 ⁺⁸⁶⁸ ₋₈₆₈	6384 ⁺⁷¹⁵ ₋₅₈₀	C IV-calibrated
SDSS J171420.38+414815.7	5948 ⁺⁸⁹² ₋₈₉₂	6725 ⁺⁸⁰⁰ ₋₆₄₂	C IV-calibrated
SDSS J212951.40-001804.3	3316 ⁺⁴⁹⁷ ₋₄₉₇	1336 ⁺⁸⁸⁸ ₋₇₉₃	C IV-calibrated
SDSS J225438.30+232714.5	6260 ⁺⁹³⁹ ₋₉₃₉	7383 ⁺⁹⁷⁷ ₋₇₇₅	C IV-calibrated

Table 2 continued

Table 2 (*continued*)

Target	$W_{90,\text{CIV}}$	$W_{90,[\text{OIII}]}$	Broad Balmer?	Fe II?	Where [O III]
	[km s ⁻¹]	[km s ⁻¹]			
(1)	(2)	(3)	(4)	(5)	(6)

NOTE—(1) SDSS identifiers. (2)–(3) The line widths encompassing 90% of the total power of the C IV λ 1549 and [O III] λ 5008 emission lines, respectively. (4) Does the source show broad Balmer emission lines in its rest-frame optical spectrum? (5) Does the source show Fe II pseudo-continuum? (6) How is the $W_{90,[\text{OIII}]}$ obtained? “FIRE” and “P19” represent direct measurement from our FIRE observation or the rest-frame optical spectra from [Perrotta et al. \(2019\)](#), respectively, and “C IV-calibrated” represents that $W_{90,[\text{OIII}]}$ is inferred from $W_{90,\text{CIV}}$.

Table 3. X-ray Measurements of Extremely Red Quasars

Target	t_{exp} [ks]	$C_{\text{net}}^{0.3-1}$	C_{net}^{1-4}	C_{net}^{4-7}	$C_{\text{net}}^{0.3-7}$	HR ₁	HR ₂	HR?	$\log N_{\text{H}}$ [cm ⁻²]	$L_{\text{X,abs}}^{2-10\text{keV}}$ [erg s ⁻¹]	$L_{\text{X,int}}^{2-10\text{keV}}$ [erg s ⁻¹]
(1)	(2)	(3)	(4)	(5)	(6)	(7)	(8)	(9)	(10)	(11)	(12)
J0024+2450	4.1	< 6.77	< 6.85	< 6.77	< 6.90	< 44.52	< 45.39
J0047+2640	20.2	< 6.95	< 7.53	< 7.31	< 8.24	< 43.86	< 44.73
J0050-0212	20.9	< 6.87	< 7.23	< 7.11	5.60 ± 2.45	< 25.0	< 43.76	< 44.10
J0116-0505	70.1	< 7.46	45.39 ± 6.78	25.36 ± 5.10	71.46 ± 8.54	0.97 ^{+0.03} _{-0.02}	-0.28 ^{+0.11} _{-0.12}	2	24.1 ^{+0.1} _{-0.1}	44.30 ^{+0.07} _{-0.08}	45.27 ^{+0.08} _{-0.09}
J0152+3231	4.1	< 6.82	< 6.79	< 6.85	< 6.98	< 44.52	< 45.39
J0805+4541	4.1	< 6.79	< 7.36	< 6.87	< 7.53	< 44.45	< 45.32
J0826+5653	19.8	< 6.90	7.71 ± 2.83	3.91 ± 2.00	11.55 ± 3.46	0.96 ^{+0.04} _{-0.06}	-0.32 ^{+0.25} _{-0.29}	2	23.8 ^{+0.2} _{-0.5}	44.05 ^{+0.09} _{-0.09}	44.72 ^{+0.16} _{-0.26}
J0826+1639	22.1	2.86 ± 1.73	16.65 ± 4.12	< 7.26	22.30 ± 4.80	0.70 ^{+0.18} _{-0.13}	-0.71 ^{+0.13} _{-0.18}	2	22.7 ^{+0.7} _{-2.7}	44.43 ^{+0.05} _{-0.08}	44.56 ^{+0.17} _{-0.06}
J0854+1730	21.1	< 6.90	< 7.55	< 7.18	< 8.10	< 43.86	< 44.72
J0958+5000	17.6	< 6.85	3.84 ± 2.00	< 7.05	5.68 ± 2.45	0.92 ^{+0.08} _{-0.12}	-0.34 ^{+0.33} _{-0.42}	2	23.8 ^{+0.3} _{-3.8}	43.78 ^{+0.22} _{-0.13}	44.44 ^{+0.21} _{-0.43}
J1013+3427	4.1	< 6.74	2.96 ± 1.73	< 6.77	2.95 ± 1.73	0.89 ^{+0.11} _{-0.15}	-0.89 ^{+0.15} _{-0.11}	1	23.0 ^{+2.0} _{-0.7}	44.27 ^{+0.05} _{-2.79}	44.47 ^{+1.54} _{-0.28}
J1021+2144	20.8	< 6.95	22.75 ± 4.80	< 6.98	25.57 ± 5.10	0.92 ^{+0.07} _{-0.05}	-0.84 ^{+0.08} _{-0.12}	1	22.5 ^{+0.7} _{-2.5}	44.49 ^{+0.03} _{-0.09}	44.57 ^{+0.24} _{-0.05}
J1025+2454	9.9	< 6.87	< 7.08	< 6.85	< 7.31	< 44.10	< 44.97
J1034+1430	23.5	< 6.95	< 7.21	< 7.16	< 7.80	< 43.86	< 44.73
J1046+0243	4.1	< 6.79	< 6.85	< 6.74	< 6.90	< 44.51	< 45.38
J1047+4844	4.1	< 6.79	< 6.87	1.99 ± 1.41	2.92 ± 1.73	...	0.34 ^{+0.59} _{-0.30}	2	24.3 ^{+0.7} _{-0.2}	43.75 ^{+0.21} _{-2.24}	45.23 ^{+0.81} _{-0.20}
J1047+6213	24.1	< 6.90	11.83 ± 3.46	< 6.98	12.68 ± 3.61	0.98 ^{+0.02} _{-0.04}	-0.85 ^{+0.08} _{-0.15}	1	23.3 ^{+1.7} _{-0.5}	44.15 ^{+0.07} _{-2.81}	44.49 ^{+1.38} _{-0.11}
J1102-0007	26.6	< 6.98	31.62 ± 5.66	6.77 ± 2.65	38.30 ± 6.25	0.99 ^{+0.01} _{-0.01}	-0.64 ^{+0.11} _{-0.13}	2	23.2 ^{+0.3} _{-3.2}	44.62 ^{+0.14} _{-0.06}	44.92 ^{+0.11} _{-0.15}
J1117+4623	4.1	5.99 ± 2.45	22.94 ± 4.80	2.99 ± 1.73	31.92 ± 5.66	0.58 ^{+0.16} _{-0.13}	-0.76 ^{+0.10} _{-0.14}	2	22.6 ^{+0.6} _{-2.6}	45.21 ^{+0.03} _{-0.04}	45.31 ^{+0.15} _{-0.07}
J1138+4732	4.1	< 6.90	< 6.85	< 6.77	< 7.03	< 44.43	< 45.30
J1217+0234	3.9	< 6.74	< 6.95	1.98 ± 1.41	2.90 ± 1.73	...	0.36 ^{+0.56} _{-0.26}	2	24.4 ^{+0.6} _{-0.2}	43.71 ^{+0.24} _{-2.19}	45.32 ^{+0.72} _{-0.18}
J1232+0912	10.8	< 6.90	< 7.05	< 7.00	< 7.46	< 44.06	< 44.93
J1254+2104	4.1	< 6.79	3.94 ± 2.00	< 6.79	3.90 ± 2.00	0.92 ^{+0.08} _{-0.11}	-0.92 ^{+0.11} _{-0.08}	1	23.3 ^{+1.7} _{-0.5}	44.54 ^{+0.09} _{-2.98}	44.87 ^{+1.21} _{-0.10}
J1307+3648	39.5	< 8.77	20.36 ± 4.90	< 11.67	24.09 ± 5.57	0.83 ^{+0.14} _{-0.08}	-0.88 ^{+0.08} _{-0.12}	1	22.8 ^{+0.6} _{-0.3}	44.15 ^{+0.01} _{-0.02}	44.30 ^{+0.19} _{-0.05}
J1309+5601	4.1	< 6.87	< 6.85	< 6.79	< 7.03	< 44.48	< 45.35
J1342+6056	17.1	< 6.85	10.81 ± 3.32	< 6.92	12.70 ± 3.61	0.82 ^{+0.17} _{-0.09}	-0.83 ^{+0.09} _{-0.15}	1	< 25.0	< 41.51	< 46.03

Table 3 continued

Table 3 (continued)

Target	t_{exp} [ks]	$C_{\text{net}}^{0.3-1}$	C_{net}^{1-4}	C_{net}^{4-7}	$C_{\text{net}}^{0.3-7}$	HR ₁	HR ₂	HR?	$\log N_{\text{H}}$ [cm ⁻²]	$L_{\text{X,abs}}^{2-10\text{keV}}$ [erg s ⁻¹]	$L_{\text{X,int}}^{2-10\text{keV}}$ [erg s ⁻¹]
(1)	(2)	(3)	(4)	(5)	(6)	(7)	(8)	(9)	(10)	(11)	(12)
J1344+4454	4.1	< 6.77	< 6.82	< 6.95	< 7.05	< 44.57	< 45.44
J1344+1401	25.7	< 6.90	< 7.38	< 7.21	< 7.96	< 43.78	< 44.65
J1345+6000	21.8	< 6.82	6.67 ± 2.65	< 7.03	6.52 ± 2.65	0.95 ^{+0.05} _{-0.07}	-0.95 ^{+0.07} _{-0.05}	1	23.2 ^{+1.8} _{-1.1}	44.04 ^{+0.13} _{-2.98}	44.32 ^{+1.27} _{-0.10}
J1348-0250	13.3	< 6.87	5.89 ± 2.45	3.94 ± 2.00	9.77 ± 3.16	0.95 ^{+0.05} _{-0.08}	-0.19 ^{+0.28} _{-0.31}	2	23.9 ^{+0.2} _{-0.4}	44.08 ^{+0.09} _{-0.11}	44.86 ^{+0.17} _{-0.24}
J1355+1447	4.1	< 6.79	< 6.85	< 6.79	< 6.95	< 44.50	< 45.37
J1456+2145	21.1	2.86 ± 1.73	19.75 ± 4.47	4.92 ± 2.24	27.53 ± 5.29	0.74 ^{+0.16} _{-0.11}	-0.59 ^{+0.14} _{-0.17}	2	23.4 ^{+0.3} _{-3.4}	44.51 ^{+0.15} _{-0.05}	44.88 ^{+0.13} _{-0.21}
J1501+2317	20.8	< 6.87	< 7.28	< 7.11	< 7.75	< 43.93	< 44.79
J1531+1058	19.2	< 6.95	< 7.26	< 7.03	< 7.72	< 43.90	< 44.77
J1542+1020	4.1	< 6.79	< 6.87	< 6.74	< 6.92	< 44.60	< 45.47
J1550+0806	17.1	< 6.87	< 7.03	3.92 ± 2.00	6.75 ± 2.65	...	0.34 ^{+0.41} _{-0.32}	2	24.4 ^{+0.6} _{-0.3}	43.42 ^{+0.32} _{-2.20}	45.06 ^{+0.68} _{-0.25}
J1604+5633	4.1	< 6.77	< 6.85	< 6.85	< 6.98	< 44.46	< 45.33
J1714+4148	22.8	< 7.08	< 7.46	< 7.08	< 8.07	< 43.75	< 44.62
J2254+2327	25.6	< 6.95	3.68 ± 2.00	< 7.33	5.35 ± 2.45	0.91 ^{+0.09} _{-0.12}	-0.35 ^{+0.34} _{-0.44}	2	23.9 ^{+0.3} _{-3.9}	43.72 ^{+0.37} _{-0.27}	44.50 ^{+0.24} _{-0.40}
J2323-0100	14.9	< 6.98	< 7.18	< 7.08	< 7.72	< 43.93	< 44.80

NOTE—(1) The target name in the SDSS HHMM±DDMM format. (2) Exposure times. (3)–(5) Net counts within the observed 0.3–1 keV, 1–4 keV, and 4–7 keV bands. (6)–(7) Hardness ratios defined by Equations 1 and 2. (8) Which HR is used to estimate gas column density? (9) Gas column densities. (10) X-ray luminosities within rest-frame 2–10 keV before correcting for gas absorption. (11) Intrinsic X-ray luminosities within rest-frame 2–10 keV after gas absorption correction.

NOTE—BEHR is able to compute HRs even if one of the two bands is undetected. Hence, HR values are not presented only for sources that are undetected in both relevant energy bands.

REFERENCES

- Alexandroff, R. M., Zakamska, N. L., Barth, A. J., et al. 2018, *MNRAS*, 479, 4936, doi: [10.1093/mnras/sty1685](https://doi.org/10.1093/mnras/sty1685)
- Baskin, A., & Laor, A. 2005, *MNRAS*, 356, 1029, doi: [10.1111/j.1365-2966.2004.08525.x](https://doi.org/10.1111/j.1365-2966.2004.08525.x)
- Boyle, B. J., & Terlevich, R. J. 1998, *MNRAS*, 293, L49, doi: [10.1046/j.1365-8711.1998.01264.x](https://doi.org/10.1046/j.1365-8711.1998.01264.x)
- Bridge, C. R., Blain, A., Borys, C. J. K., et al. 2013, *ApJ*, 769, 91, doi: [10.1088/0004-637X/769/2/91](https://doi.org/10.1088/0004-637X/769/2/91)
- Cano-Díaz, M., Maiolino, R., Marconi, A., et al. 2012, *A&A*, 537, L8, doi: [10.1051/0004-6361/201118358](https://doi.org/10.1051/0004-6361/201118358)
- Castor, J. I., Abbott, D. C., & Klein, R. I. 1975, *ApJ*, 195, 157, doi: [10.1086/153315](https://doi.org/10.1086/153315)
- Chen, C.-T. J., Hickox, R. C., Goulding, A. D., et al. 2017, *ApJ*, 837, 145, doi: [10.3847/1538-4357/837/2/145](https://doi.org/10.3847/1538-4357/837/2/145)
- Croton, D. J., Springel, V., White, S. D. M., et al. 2006, *MNRAS*, 365, 11, doi: [10.1111/j.1365-2966.2005.09675.x](https://doi.org/10.1111/j.1365-2966.2005.09675.x)
- Dawson, K. S., Schlegel, D. J., Ahn, C. P., et al. 2013, *AJ*, 145, 10, doi: [10.1088/0004-6256/145/1/10](https://doi.org/10.1088/0004-6256/145/1/10)
- Dopita, M. A., Groves, B. A., Sutherland, R. S., Binette, L., & Cecil, G. 2002, *ApJ*, 572, 753, doi: [10.1086/340429](https://doi.org/10.1086/340429)
- Eisenhardt, P. R. M., Wu, J., Tsai, C.-W., et al. 2012, *ApJ*, 755, 173, doi: [10.1088/0004-637X/755/2/173](https://doi.org/10.1088/0004-637X/755/2/173)
- Finnerty, L., Larson, K., Soifer, B. T., et al. 2020, *ApJ*, 905, 16, doi: [10.3847/1538-4357/abc3bf](https://doi.org/10.3847/1538-4357/abc3bf)
- Förster Schreiber, N. M., Übler, H., Davies, R. L., et al. 2019, *ApJ*, 875, 21, doi: [10.3847/1538-4357/ab0ca2](https://doi.org/10.3847/1538-4357/ab0ca2)
- Fruscione, A., McDowell, J. C., Allen, G. E., et al. 2006, in *Society of Photo-Optical Instrumentation Engineers (SPIE) Conference Series*, Vol. 6270, *Observatory Operations: Strategies, Processes, and Systems*, ed. D. R. Silva & R. E. Doxsey, 62701V, doi: [10.1117/12.671760](https://doi.org/10.1117/12.671760)
- Gandhi, P., Horst, H., Smette, A., et al. 2009, *A&A*, 502, 457, doi: [10.1051/0004-6361/200811368](https://doi.org/10.1051/0004-6361/200811368)
- Gehrels, N. 1986, *ApJ*, 303, 336, doi: [10.1086/164079](https://doi.org/10.1086/164079)
- Gillette, J., Hamann, F., Lau, M. W., & Perrotta, S. 2023, *MNRAS*, doi: [10.1093/mnras/stad2890](https://doi.org/10.1093/mnras/stad2890)
- Girelli, G., Bolzonella, M., & Cimatti, A. 2019, *A&A*, 632, A80, doi: [10.1051/0004-6361/201834547](https://doi.org/10.1051/0004-6361/201834547)
- Goulding, A. D., Zakamska, N. L., Alexandroff, R. M., et al. 2018, *ApJ*, 856, 4, doi: [10.3847/1538-4357/aab040](https://doi.org/10.3847/1538-4357/aab040)
- Gräfenor, G., Owocki, S. P., Grassitelli, L., & Langer, N. 2017, *A&A*, 608, A34, doi: [10.1051/0004-6361/201731590](https://doi.org/10.1051/0004-6361/201731590)
- Greene, J. E., Zakamska, N. L., & Smith, P. S. 2012, *ApJ*, 746, 86, doi: [10.1088/0004-637X/746/1/86](https://doi.org/10.1088/0004-637X/746/1/86)
- Hamann, F., Zakamska, N. L., Ross, N., et al. 2017, *MNRAS*, 464, 3431, doi: [10.1093/mnras/stw2387](https://doi.org/10.1093/mnras/stw2387)
- Harrison, C. M., Alexander, D. M., Mullaney, J. R., et al. 2016, *MNRAS*, 456, 1195, doi: [10.1093/mnras/stv2727](https://doi.org/10.1093/mnras/stv2727)
- Heckman, T. M., & Best, P. N. 2014, *ARA&A*, 52, 589, doi: [10.1146/annurev-astro-081913-035722](https://doi.org/10.1146/annurev-astro-081913-035722)
- Heckman, T. M., Krolik, J. H., Moran, S. M., Schnittman, J., & Gezari, S. 2009, *ApJ*, 695, 363, doi: [10.1088/0004-637X/695/1/363](https://doi.org/10.1088/0004-637X/695/1/363)
- Hopkins, P. F., Hernquist, L., Cox, T. J., et al. 2006, *ApJS*, 163, 1, doi: [10.1086/499298](https://doi.org/10.1086/499298)
- Hwang, H.-C., Zakamska, N. L., Alexandroff, R. M., et al. 2018, *MNRAS*, 477, 830, doi: [10.1093/mnras/sty742](https://doi.org/10.1093/mnras/sty742)
- Ishibashi, W., Banerji, M., & Fabian, A. C. 2017, *MNRAS*, 469, 1496, doi: [10.1093/mnras/stx921](https://doi.org/10.1093/mnras/stx921)
- Ishibashi, W., Fabian, A. C., & Maiolino, R. 2018, *MNRAS*, 476, 512, doi: [10.1093/mnras/sty236](https://doi.org/10.1093/mnras/sty236)
- Ishikawa, Y., Goulding, A. D., Zakamska, N. L., et al. 2021, *MNRAS*, 502, 3769, doi: [10.1093/mnras/stab137](https://doi.org/10.1093/mnras/stab137)
- Ito, K., Tanaka, M., Valentino, F., et al. 2023, *ApJL*, 945, L9, doi: [10.3847/2041-8213/acb49b](https://doi.org/10.3847/2041-8213/acb49b)
- Jiang, Y.-F., Stone, J. M., & Davis, S. W. 2019, *ApJ*, 880, 67, doi: [10.3847/1538-4357/ab29ff](https://doi.org/10.3847/1538-4357/ab29ff)
- Keating, S. K., Everett, J. E., Gallagher, S. C., & Deo, R. P. 2012, *ApJ*, 749, 32, doi: [10.1088/0004-637X/749/1/32](https://doi.org/10.1088/0004-637X/749/1/32)
- Kelly, B. C. 2007, *ApJ*, 665, 1489, doi: [10.1086/519947](https://doi.org/10.1086/519947)
- King, A. 2003, *ApJL*, 596, L27, doi: [10.1086/379143](https://doi.org/10.1086/379143)
- Komossa, S. 2012, *Advances in Astronomy*, 2012, 364973, doi: [10.1155/2012/364973](https://doi.org/10.1155/2012/364973)
- Komossa, S., Xu, D., Zhou, H., Storchi-Bergmann, T., & Binette, L. 2008, *ApJ*, 680, 926, doi: [10.1086/587932](https://doi.org/10.1086/587932)
- Leung, G. C. K., Coil, A. L., Aird, J., et al. 2019, *ApJ*, 886, 11, doi: [10.3847/1538-4357/ab4a7c](https://doi.org/10.3847/1538-4357/ab4a7c)
- Luo, B., Brandt, W. N., Alexander, D. M., et al. 2014, *ApJ*, 794, 70, doi: [10.1088/0004-637X/794/1/70](https://doi.org/10.1088/0004-637X/794/1/70)
- Lusso, E., Nardini, E., Bisogni, S., et al. 2021, *A&A*, 653, A158, doi: [10.1051/0004-6361/202141356](https://doi.org/10.1051/0004-6361/202141356)
- Lusso, E., Nardini, E., Fumagalli, M., et al. 2023, *MNRAS*, doi: [10.1093/mnras/stad2564](https://doi.org/10.1093/mnras/stad2564)
- Madau, P., & Dickinson, M. 2014, *ARA&A*, 52, 415, doi: [10.1146/annurev-astro-081811-125615](https://doi.org/10.1146/annurev-astro-081811-125615)
- Marinello, M., Rodríguez-Ardila, A., García-Rissmann, A., Sigut, T. A. A., & Pradhan, A. K. 2016, *ApJ*, 820, 116, doi: [10.3847/0004-637X/820/2/116](https://doi.org/10.3847/0004-637X/820/2/116)
- Mateos, S., Carrera, F. J., Alonso-Herrero, A., et al. 2015, *MNRAS*, 449, 1422, doi: [10.1093/mnras/stv299](https://doi.org/10.1093/mnras/stv299)
- Murray, N., Chiang, J., Grossman, S. A., & Voit, G. M. 1995, *ApJ*, 451, 498, doi: [10.1086/176238](https://doi.org/10.1086/176238)
- Osterbrock, D. E. 1991, *Reports on Progress in Physics*, 54, 579, doi: [10.1088/0034-4885/54/4/002](https://doi.org/10.1088/0034-4885/54/4/002)
- Pâris, I., Petitjean, P., Aubourg, É., et al. 2014, *A&A*, 563, A54, doi: [10.1051/0004-6361/201322691](https://doi.org/10.1051/0004-6361/201322691)

- Pâris, I., Petitjean, P., Ross, N. P., et al. 2017, *A&A*, 597, A79, doi: [10.1051/0004-6361/201527999](https://doi.org/10.1051/0004-6361/201527999)
- Park, T., Kashyap, V. L., Siemiginowska, A., et al. 2006, *ApJ*, 652, 610, doi: [10.1086/507406](https://doi.org/10.1086/507406)
- Perrotta, S., Hamann, F., Zakamska, N. L., et al. 2019, *MNRAS*, 488, 4126, doi: [10.1093/mnras/stz1993](https://doi.org/10.1093/mnras/stz1993)
- Prochaska, J. X., Hennawi, J. F., Westfall, K. B., et al. 2020a, arXiv e-prints, arXiv:2005.06505. <https://arxiv.org/abs/2005.06505>
- Prochaska, J. X., Hennawi, J., Cooke, R., et al. 2020b, pypeit/PypeIt: Release 1.0.0, v1.0.0, Zenodo, doi: [10.5281/zenodo.3743493](https://doi.org/10.5281/zenodo.3743493)
- Proga, D. 2005, *ApJL*, 630, L9, doi: [10.1086/462417](https://doi.org/10.1086/462417)
- Proga, D., & Kallman, T. R. 2004, *ApJ*, 616, 688, doi: [10.1086/425117](https://doi.org/10.1086/425117)
- Proga, D., Stone, J. M., & Drew, J. E. 1999, *MNRAS*, 310, 476, doi: [10.1046/j.1365-8711.1999.02935.x](https://doi.org/10.1046/j.1365-8711.1999.02935.x)
- Proga, D., Stone, J. M., & Kallman, T. R. 2000, *ApJ*, 543, 686, doi: [10.1086/317154](https://doi.org/10.1086/317154)
- Ricci, C., Assef, R. J., Stern, D., et al. 2017, *ApJ*, 835, 105, doi: [10.3847/1538-4357/835/1/105](https://doi.org/10.3847/1538-4357/835/1/105)
- Richards, G. T., Lacy, M., Storrie-Lombardi, L. J., et al. 2006, *ApJS*, 166, 470, doi: [10.1086/506525](https://doi.org/10.1086/506525)
- Richards, G. T., Kruczek, N. E., Gallagher, S. C., et al. 2011, *AJ*, 141, 167, doi: [10.1088/0004-6256/141/5/167](https://doi.org/10.1088/0004-6256/141/5/167)
- Ross, N. P., Hamann, F., Zakamska, N. L., et al. 2015, *MNRAS*, 453, 3932, doi: [10.1093/mnras/stv1710](https://doi.org/10.1093/mnras/stv1710)
- Shlosman, I., Vitello, P. A., & Shaviv, G. 1985, *ApJ*, 294, 96, doi: [10.1086/163278](https://doi.org/10.1086/163278)
- Silk, J., & Rees, M. J. 1998, *A&A*, 331, L1, doi: [10.48550/arXiv.astro-ph/9801013](https://doi.org/10.48550/arXiv.astro-ph/9801013)
- Stern, D. 2015, *ApJ*, 807, 129, doi: [10.1088/0004-637X/807/2/129](https://doi.org/10.1088/0004-637X/807/2/129)
- Sulentic, J. W., del Olmo, A., Marziani, P., et al. 2017, *A&A*, 608, A122, doi: [10.1051/0004-6361/201630309](https://doi.org/10.1051/0004-6361/201630309)
- Thompson, T. A., Fabian, A. C., Quataert, E., & Murray, N. 2015, *MNRAS*, 449, 147, doi: [10.1093/mnras/stv246](https://doi.org/10.1093/mnras/stv246)
- Tsai, C.-W., Eisenhardt, P. R. M., Wu, J., et al. 2015, *ApJ*, 805, 90, doi: [10.1088/0004-637X/805/2/90](https://doi.org/10.1088/0004-637X/805/2/90)
- Vayner, A., Zakamska, N. L., Riffel, R. A., et al. 2021, *MNRAS*, 504, 4445, doi: [10.1093/mnras/stab1176](https://doi.org/10.1093/mnras/stab1176)
- Vayner, A., Zakamska, N. L., Ishikawa, Y., et al. 2023, arXiv e-prints, arXiv:2303.06970, doi: [10.48550/arXiv.2303.06970](https://doi.org/10.48550/arXiv.2303.06970)
- Veilleux, S., Cecil, G., & Bland-Hawthorn, J. 2005, *ARA&A*, 43, 769, doi: [10.1146/annurev.astro.43.072103.150610](https://doi.org/10.1146/annurev.astro.43.072103.150610)
- Véron-Cetty, M. P., Joly, M., & Véron, P. 2004, *A&A*, 417, 515, doi: [10.1051/0004-6361:20035714](https://doi.org/10.1051/0004-6361:20035714)
- Vito, F., Brandt, W. N., Stern, D., et al. 2018, *MNRAS*, 474, 4528, doi: [10.1093/mnras/stx3120](https://doi.org/10.1093/mnras/stx3120)
- Weisskopf, M. C., Wu, K., Trimble, V., et al. 2007, *ApJ*, 657, 1026, doi: [10.1086/510776](https://doi.org/10.1086/510776)
- Wright, E. L., Eisenhardt, P. R. M., Mainzer, A. K., et al. 2019, AllWISE Source Catalog, IPAC, doi: [10.26131/IRSA1](https://doi.org/10.26131/IRSA1)
- Wu, J., Tsai, C.-W., Sayers, J., et al. 2012, *ApJ*, 756, 96, doi: [10.1088/0004-637X/756/1/96](https://doi.org/10.1088/0004-637X/756/1/96)
- Wu, J., Jun, H. D., Assef, R. J., et al. 2018, *ApJ*, 852, 96, doi: [10.3847/1538-4357/aa9ff3](https://doi.org/10.3847/1538-4357/aa9ff3)
- Wylezalek, D., Vayner, A., Rupke, D. S. N., et al. 2022, *ApJL*, 940, L7, doi: [10.3847/2041-8213/ac98c3](https://doi.org/10.3847/2041-8213/ac98c3)
- Yaqoob, T. 2012, *MNRAS*, 423, 3360, doi: [10.1111/j.1365-2966.2012.21129.x](https://doi.org/10.1111/j.1365-2966.2012.21129.x)
- Zakamska, N. L., & Alexandroff, R. M. 2023, *MNRAS*, 525, 2716, doi: [10.1093/mnras/stad2474](https://doi.org/10.1093/mnras/stad2474)
- Zakamska, N. L., & Greene, J. E. 2014, *MNRAS*, 442, 784, doi: [10.1093/mnras/stu842](https://doi.org/10.1093/mnras/stu842)
- Zakamska, N. L., Strauss, M. A., Krolik, J. H., et al. 2003, *AJ*, 126, 2125, doi: [10.1086/378610](https://doi.org/10.1086/378610)
- Zakamska, N. L., Hamann, F., Pâris, I., et al. 2016, *MNRAS*, 459, 3144, doi: [10.1093/mnras/stw718](https://doi.org/10.1093/mnras/stw718)
- Zakamska, N. L., Sun, A.-L., Strauss, M. A., et al. 2019, *MNRAS*, 489, 497, doi: [10.1093/mnras/stz2071](https://doi.org/10.1093/mnras/stz2071)